Cas9/sgRNA selective targeting of the P23H *Rhodopsin* mutant allele for treating Retinitis Pigmentosa by intravitreal AAV9.PHP.B-based delivery

Serena G. Giannelli[1], Mirko Luoni[1], Valerio Castoldi[3], Luca Massimino[1,2], Tommaso Cabassi[1,2], Debora Angeloni[4], Giancarlo Demontis[5], Letizia Leocani[3], Massimiliano Andreazzoli[6], Vania Broccoli[1,2,*]

[1]Stem Cell and Neurogenesis Unit, Division of Neuroscience, San Raffaele Scientific Institute, 20132 Milan, Italy; [2]National Research Council (CNR) Institute of Neuroscience, 20129 Milan, Italy; [3]Experimental Neurophysiology Unit, Institute of Experimental Neurology (INSPE), Scientific Institute Hospital San Raffaele, Milan Italy; [4]Institute of Life Sciences, Scuola Superiore Sant'Anna, 56124 Pisa, Italy; [5]Department of Pharmacy, University of Pisa Pisa, Italy; [6]Department of Biology, University of Pisa, 56127 Pisa, Italy.

*** Corresponding author:**

Vania Broccoli

Stem Cells and Neurogenesis Unit, Division of Neuroscience, San Raffaele Scientific Institute

Via Olgettina 58, 20132 Milan, Italy. Tel: +39 02 26434616; FAX +39 02 26434621.

E-mail: broccoli.vania@hsr.it. Website: *www.vaniabroccolilab.com*

Abstract

P23H is the most common mutation in the *RHODOPSIN* (*RHO*) gene leading to a dominant form of Retinitis Pigmentosa (RP), a rod photoreceptor degeneration that invariably causes vision loss. Specific disruption of the disease P23H *RHO* mutant while preserving the wild-type functional allele would be an invaluable therapy for this disease. However, various technologies tested in the past failed to achieve effective changes and consequently therapeutic benefits. We validated a CRISPR/Cas9 strategy to specifically inactivate the P23H *RHO* mutant, while preserving the wild-type (WT) allele *in vitro*. We, then, translated this approach *in vivo* by delivering the CRISPR/Cas9 components in murine $Rho^{+/P23H}$ mutant retinae. Targeted retinae presented a high rate of cleavage in the P23H but not WT *Rho* allele. This gene manipulation was sufficient to slow photoreceptor degeneration and improve retinal functions. In order improve the translational potential of our approach we tested intravitreal delivery of this system by means of adeno-associated viruses (AAVs). To this purpose the employment of the AAV9-PHP.B resulted the most effective in disrupting the P23H *Rho* mutant. Finally, this approach was translated successfully in human cells engineered with the homozygous P23H *RHO* gene mutation. Overall, this is a significant proof-of-concept that gene allele specific targeting by CRISPR/Cas9 technology is specific and efficient and represents an unprecedented tool for treating RP and more broadly dominant genetic human disorders affecting the eye, as well as other tissues.

Introduction

Retinitis pigmentosa (RP) is the most common cause of blindness and includes a large number of inherited retinal disorders (1). RP causes a primary rod photoreceptor cell death associated to night blindness with visual field restriction, followed by cone cell deterioration and loss of central vision. More than 60 genes have been identified to cause RP (2–4) and inherited in autosomal recessive (arRP) (5), dominant (adRP) (6–8) and X-linked (xRP) (9) genetic traits. Among the relatively large number of genetic loci causing adRPs, the *RHODOPSIN* (*RHO*) gene is the most prominent, accounting for 15% of retinal degenerations and 25% of adRP (10, 11). *RHO* encodes for a rod receptor protein that, binding to retinal, can sense light and initiate the phototransduction cascade in rod photoreceptors (12). Among the 120 mutations identified in *RHO*, the p.Pro23Hist (P23H) is the most frequent mutation which alone accounts for about 10% of the adRP cases in north America. In animal models, this mutation causes gain-of-function pathological effects inducing Rhodopsin protein misfolding, aggregation and reduced glycosylation (13, 14), thus leading to rod death and retinal impairment (15, 16). In addition, the P23H mutant Rho protein was shown to destabilize rod photoreceptor disk membranes and interfere with the disc membrane reorientation process (17, 18)

Currently, no therapies are available to halt or delay RP disease progression, nor photoreceptor cell death. However, given that the retina is an easily accessible, relative small, compartmentalized and immune privileged tissue, AAV-based methods have been particularly successful in therapeutic gene delivery. Importantly, clinical trials on severe forms of retinal dystrophies (19) have shown to be safe and rather efficacious in ameliorating patient visual acuity (20–22). Gene therapy is currently widely explored in a variety of pre-clinical studies but its application remains restricted to loss-of-function genetic diseases, in which gene replacement, even to a small degree, can account for functional restoration (23, 24). Conversely, most of the adRP forms caused by gain-of-function mutations are excluded from these developments since silencing of the mutant pathogenic allele is required for functional rescue. In this scenario allele-specific strategies are further complicated, given the hurdles posed by the discrimination between the wild-type (WT) and the mutated sequence, often reduced to a single nucleotide difference.

The recent introduction of the CRISPR/Cas9 system might provide an unprecedented tool for specific manipulation and disruption of the mutant alleles by selective allele gene targeting. This system employs the bacterial Cas9 endonuclease to cleave DNA sequences targeted by a short guide RNA “sgRNA” complementary to the ≈20nt target sequence and providing specificity to any site of the genome proximal to a fixed protospacer adjacent motif (PAM) sequence (25). Recruited by sgRNA, Cas9 proteins cleave the DNA at a fixed distance from the PAM domain, thus producing a double strand break (DBS) that triggers the endogenous DNA repair mechanisms,

including the error prone non-homologous end-joining (NHEJ) pathway, that entails small insertion and/or deletion (indel), and the high-fidelity homologous directed repair (HDR), that instead leads to targeted integration of a provided DNA donor sequence. These two pathways can be exploited respectively for targeted gene disruption or repair and modification. Although these two processes are formally equivalent, taking advantage of NHEJ is easier and more efficacious since in many cellular systems is often prevalent to HDR, especially in post-mitotic cells, and moreover it does not require a donor template (25). The most popular and optimized CRISPR/Cas9 system is based on *Streptococcus pyogens* innate immune system (SpCas9) and relies on the NGG PAM site that is fairly abundant throughout the genome but still limited. More recently the identification of different Cas9 orthologs and the development of engineered variants have provided a customizable variety of nucleases with different PAM sequence and, therefore, largely expanding the targeting range of this system across the genome (26, 27). For instance the D1135V/R1335Q/T1337R triple SpCas9 mutant protein (hereafter referred to as Cas9-VQR) was engineered to this purpose and recognizes the novel PAM site NGA (28).

In the past various paradigms of gene inactivation have been taken into consideration for *Rho* inactivation with variable degrees of specificity and efficacy: ribozymes (29, 30), short hairpin RNAs (31, 32), zinc-finger nuclease (33). Thus, we decided to take advantage of the CRISPR/Cas9 expanded genome editing capacity to achieve the specific inactivation of the P23H *Rho* allele in order to counteract the photoreceptor degeneration and disease progression. We explored this hypothesis both *in vitro* and *in vivo*, using the P23H knock-in mouse line, which represents a faithful animal model of the human disease, closely recapitulating the dynamics and pathological progression of the human retinal degeneration (34). Here, we demonstrated for the first time that the selective and efficient inactivation of the P23H *Rho* mutant allele in the retinal tissue upon *in vivo* SpCas9 variant delivery mediated either by plasmidic DNA transduction or AAVs. These results provide a strong proof-of-concept for the therapeutic exploitation of this system that aims to minimize photoreceptor degeneration and visual loss.

Results

Targeting of the P23H *Rho* allele based on the CRISPR/SpCas9-VQR system

The P23H mutation is due to the pathogenic C-to-A nucleotide transversion in position 68 of the *Rho* coding sequence, both in human and mice. We asked whether this mutation could generate a novel protospacer adjacent motif (neo-PAM) for one of the various Cas9 protein orthologs or variants, thus providing selectivity for the mutated allele. Intriguingly, we found a NNHRRT PAM

domain that overlapped precisely with the A68 nucleotide on the antiparallel strand of both human and murine *Rho* gene (sgRNA-saC1) (**Fig. S1**). This PAM site is specific for the newly discovered variant of the *Streptococcus Aureus* Cas9 (SaCas9-KHH) that for its smaller size is more apt for translational purposes (35, 36). We mounted the SaCas9-KHH in a lentiviral vector equipped with the puromycin resistance gene (Puro) and the sgRNA-saC1 in a second vector containing the sgRNA scaffold optimized for SaCas9 and the resistance gene for blastidicin (Blast). We used WT and P23H *Rho* Mouse Embryonic Fibroblasts (MEFs) to test if this guide could selectively cleave the P23H *Rho* mutant allele even in double Blast/Puro resistant MEFs. Unfortunately no detectable cleavage was found either at the level of WT or P23H *Rho* sequence using two different methods for indel assessment, namely the T7 endonuclease I (T7EI) assay and the Tracking of Indels by DEcomposition (TIDE) analysis (37) (**Fig. S2**). By contrast, the same vectors equipped with a published guide targeting the *EMX1* gene (26) led to a significant DNA cleavage in 293T cells even in absence of antibiotic selection, thus excluding technical issues (**Fig. S2**). Since it is known that sgRNA specificity is depending by its seed sequence, a stretch of 8 to 14 nucleotides before the PAM domain (38, 39), we focused on specific sgRNAs whose seed sequences included the P23H mutation, and the relative PAMs were conserved between human and mouse. Interestingly, we found in the proximity of the c.68C>A mutation a second NNHRRT PAM domain (sgRNA-saC2) and also an NGA PAM sequence, which is targeted by the Cas9-VQR (sgRNA-mMUT) (**Fig. S1**). Since sgRNA-saC2 similarly to sgRNA-saC1 resulted ineffective (**Fig. S2**), we decided to take advantage of the NGA PAM site and we designed the sgRNA-mMUT complementary to the mutant, but bearing a single mismatch to the WT *Rho* allele (**Fig. S3A,B**). For this purpose, we generated lentiviral vectors equipped with either one of the two SpCas9 (WT and VQR) and Puro; the sgRNA-mMUT, expressing the sgRNA in association to the proper scaffold together with the Blast gene resistance; and finally both CRISPR/Cas9 elements were mounted on the same vector in order to take advantage of the single selection for Puro. The two former vectors together or the last one alone were tested in $Rho^{+/+}$ or $Rho^{P23H/P23H}$ MEFs using appropriate selections. Two days after infection cleavage efficiency was measured using the T7EI assay. Notably, while in WT samples indel mutations were not detected (**Fig. S3C**), a significant amount of indel (≈20-30%) was scored in P23H samples (**Fig. S3D**). Thus, the sgRNA-mMUT enabled to discriminate between the two *Rho* alleles, targeting exclusively the c.68C>A *Rho* mutant allele. Coupling the Cas9-VQR with an unspecific guide with NGG PAM selectivity or the canonical SpCas9 with the LV-U6-sgRNA-mMUT did not result in detectable cleavage (**Fig. 3D**), thus confirming PAM specificity of the SpCas9 employed. Multiple assays can be used to detect cleavage efficiency, each of them showing a different degree of accuracy (closeness to the effective value) or reproducibility (repeatability of

the measurement). In fact, molecular cloning of the targeted genomic region coupled with Sanger sequencing (here referred as clone sequencing) is the most accurate, but it's a slow and labour intensive option. On the contrary, T7EI assay is the least accurate (cleavage underestimation has been frequently reported with this assay, i.e. (40)), but very reproducible, rapid and inexpensive, thus helpful when comparing different conditions. Finally, the TIDE computational method is repeatable and convenient but not as accurate as clone sequencing. We used all these methods to complement and validate each other in order to reach the most reliable description of the introduced genetic modifications. Thus, we re-assessed sgRNA-mMUT specificity using the TIDE system (**Fig. S3E and F**). With this analysis, infected WT MEFs resulted only minimally affected (6 ± 3%) while a substantial fraction of the mutant cells accumulated targeted mutations in P23H MEFs with an overall efficiency of 65 ± 3%. Finally, molecular cloning of the targeted genomic region coupled with Sanger sequencing (clone sequencing) was exploited for a more accurate assessment of editing events. This approach failed to detect any indel mutations in WT cells (**Fig. S3G**) whereas many mutations, of various types, accumulated in mutant cells (66%) (**Fig. S1H and I**). Overall according to clone sequencing, the sgRNA-mMUT discriminated with high degree of specificity the c.68C>A mutant from the WT *Rho* sequence. Specificity of this guide was assessed also in terms of off-target activity. In fact, four of the most likely off-target sites predicted by the webtool COSMID (*https://crispr.bme.gatech.edu*) (41), were sequenced and subjected to TIDE analysis and clone sequencing but no detectable off-target indels were ascertained (**Fig. S4A**).

Estimate of WT or P23H *Rho* allele cleavage in *Rho*$^{+/P23H}$ genomic background

Sequence specificity of the sgRNA-mMUT was easily assessed on either WT or homozygous P23H mutant *Rho* genetic background. However, the same analysis would be far less informative in the *Rho*$^{+/P23H}$ genotype, which is the one associated with the human RP disease. Remarkably, the identification of a polymorphism in the *Rho* promoter region that differs between the WT and the P23H mutant allele allowed us to design two alternative forward primers to selectively amplify either of the two alleles (PCR-WT and PCR-P23H, respectively) (**Fig. S5**), thus overcoming this problem. RFLP analysis confirmed selective allele amplification with 99 and 100% specificity for PCR-WT and -P23H, respectively (**Fig. S5**). Next, our panel of cleavage efficiency measurements was applied to *Rho*$^{+/P23H}$ MEFs treated with either the sgRNA-mMUT or a corresponding guide complementary to the WT *Rho* sequence (sgRNA-mWT) in order to test cleavage also at the level of the WT allele (**Fig. S6**). T7EI assay, TIDE and clone sequencing concordantly detected significant levels of indel on the allele complementary to the guide but none when the single nucleotide mismatch was present (**Fig. S6**), thus validating the feasibility of our measurements and specificity of the selected guides.

Selective targeting of the P23H and WT *Rho* allele in *Rho*$^{+/P23H}$ murine retinae

We, then, asked whether *Rho* gene allele specific targeting could be achieved *in vivo*. To this aim we sought to deliver the CRISPR/Cas9 system components in the retinae of P0 newborn *Rho*$^{+/P23H}$ mice by *in vivo* electroporation (42). In order to efficiently target the elements of the CRISPR/Cas9-VQR system, we devised a single pCAG vector expressing the SpCas9-VQR under the strong CAG promoter and the sgRNA-mMUT under the U6 promoter. This vector was co-electroporated with a GFP reporter in the subretinal space for targeting the photoreceptor cell layer in the developing *Rho*$^{P23H/+}$ eyes (**Fig. 1A**). To assess *in vivo* efficiency and specificity of the gene allele targeting, retinae were harvested 4 weeks after electroporation and GFP^{+} cells purified by FACS-sorting followed by molecular analysis (**Fig. 1A**). We first analyzed exclusively the P23H allele by PCR-P23H amplification, and quantified the cleavage rate in 27.5 ± 1.7% for the T7EI assays (n=4) (**Fig. 1B**), but considerably higher for the TIDE analysis (**Fig. 1C**) and clone sequencing (77.2 ± 6.1%, n=4; 87.8 ± 4.5, n=3, respectively; ≈40 clones per retina) (**Fig. 1D-G**). This remarkable discrepancy in cleavage estimate between T7EI and the other methods can be explained by the over-representation of a particular Rho mutant allele with an single adenine nucleotide insertion in the P23H *Rho* sequence in edited retinae (38.1 ± 3.5 by clone sequencing, n=3) (**Fig. 1E**) that confers to the edited samples a minor degree of variability which would escape T7EI cleavage. This considered, we detected in the P23H *Rho* allele extremely high indel rate, causing frameshifts in the P23H *Rho* coding sequence in 100% of the cases (n=3) (**Fig. 1G**), which likely leads to inactivation of the disease *Rho* allele. Thus, the mutant allele targeting is not only very effective, but have also the potential to disrupt the P23H allele pathological functions, leading to the disease. In order to properly assess this issue at functional level, we cloned the 4 of most frequent *Rho* gene variants detected in our *in vivo* experiment, namely, the WT, P23H and the two most frequent indel mutants referred to as IndelA and IndelB (**Fig. 2A**) and overexpressed them in P19 mouse cells (a cell line derived from an embryonic teratocarcinoma). Previous studies has shown that in cultured epithelial HeLa cells the WT Rho protein is targeted to the cell membrane, whereas the P23H Rho protein accumulates in the endoplasmic reticulum (ER) causing severe cellular stress (43–45). Accordingly, in transfected P19 cells the WT Rho localized on the plasma membrane while the P23H mutant protein remained trapped in the cytoplasm as shown by immunofluorescence using two different antibodies recognizing the Rho N- or the C-terminal (respectively upstream and downstream the aminoacidic position 23 targeted in our editing approach). By contrast, the resulting translated products of the indelA and B *Rho* mutant alleles were undetectable using either antibody (**Fig. 2B**). These results are consistent with the premature degradation of their RNA products (**Fig. S7A and**

B) caused by nonsense-mediated decay as shown to occur with other *Rho* mutants sharing a premature termination codon (46). The presence of a premature STOP codon in both indel A and B altered proteins was indeed predicted using ORF recognitions tools (**Fig. 2A**). Moreover, possible pathogenicity associated to these frameshift mutations was assessed *in vitro* by evaluating their hypothetical ability to trigger ER stress, a significant cause underlying retinal degeneration (43). To this aim, we determined the Xbp1 spliced forms which initiates the ERAD pathway (47) using both a reporter assay and RT-PCR. Differently from the P23H mutant, the prematurely terminated forms presented basal levels of Xbp1 splicing, thus, confirming their lack of toxicity (**Fig. S7C-H**).

Next, we analyzed the mutation frequency of the WT *Rho* allele in electroporated retinae using selective amplification. In this case, T7EI analysis failed to detect significant cleavage in this allele (**Fig. 1H**) whereas TIDE analysis estimated it at 4.3 ± 0.9 (n=5) (**Fig. 1I**). Finally, according to the clone sequencing only 2 out of 3 retinae carried indel mutations (≈10%) in the WT allele (clone sequencing: ≈40 clones per retina) (**Fig. 1K-M**).

Two different retinal genomic samples were tested for off-target activity at the same sites searched previously in MEFs (41). Neither TIDE analysis nor clone sequencing, revealed any detectable off-target cleavage at these sites, thus indicating a high safety profile of this treatment (**Fig. S4B**). Overall, these results clearly outlined that the Cas9-VQR/sgRNA-mMUT system enabled an efficient and selective targeting of the P23H, mutant, capable of a high degree of inactivation in the *Rho* allele *in vivo*.

Effect of targeting of the P23H *Rho* allele in *Rho*$^{+/P23H}$ mutant retinae

Given that the *in vivo* electroporation mediated an efficient delivery of the CRISPR/Cas9 elements in the retina, with high targeting rate of the P23H mutant *Rho* allele, we wondered whether this could be sufficient to delay rod photoreceptor degeneration and especially outer segment deterioration. Outer Nuclear Layer thickness (ONL) is a surrogate for photoreceptor number, thus is an important feature to assess retinal degeneration. We measured ONL thickness in electroporated eyes (only right eyes were electroporated, RE), but since electroporation could be also detrimental to retinal integrity we also assessed it in controlateral non-electroporated eyes (left eyes, LE). Neither electroporated eyes (treated withCas9-VQR alone or Cas9-VQR toghether with sgRNAmut) nor non-electroporated eyes presented significant differences in ONL thickness (**Fig. 3A-D**). Since at one month of age photoreceptor loss in *Rho*$^{+/P23H}$ retinae is relatively mild, thus masking possible effects of our treatment, we attempted to measure other features of photoreceptor degeneration. The outer segment (OS) is the photoreceptor compartment where Rhodopsin resides, and vision initiate (12). This complex process requires a constant turn-over of molecules, proteins

and subcellular structures (48), but is also easily disrupted if one of its element, Rhodopsin among many others, is functionally altered, thus leading to retinal degeneration (49). The first hallmark of this process is OS degeneration, characterized by initial shortening, misshaping and final complete loss. Degeneration also involves inner segment (IS), the compartment that lies between the OS and the photoreceptor soma and lodges the Golgi apparatus, ER and mitochondria. 4 weeks after electroporation photoreceptor, OSs were dysmorphic in shape and shorter in control, while morphology and length was evidently more preserved in treated retinae (**Fig. 3E-Q**). Retinae treated with both Cas9-VQR and sgRNA-mMUT (CRISPR-VQR-treated) GFP^+ photoreceptor displayed longer OS/IS tract (≈150%, **Fig 3M**) than in retinae treated with the Cas9-VQR only (controls). CNGA1 (cyclic nucleotide-gated channel alpha1) and Clx (calnexin) staining were used to identify the shape respectively of the OS and IS and their relative boundaries (34), thus highlighting the differences between control and CRISPR-VQR treated retinae in the OS tract (≈190%, **Fig 3M**). Thus the OS damage induced by the $Rho^{+/P23H}$ mutation was rescued by our CRISPR/Cas9-VQR treatment.

ONL degeneration progressed at 3 months of age, moreover the detrimental effect of electroporation at this stage was clearly evident as demonstrated by ONL thickness in non-electroporated retinae (**Fig. 4A**). Despite great variability among electroporated retinae, ONL thickness was significantly lower in control compared to treated retinae (**Fig. 4B-D Fig. S8C-D**). Also OS degeneration markedly advanced at this stage to the point that in control retinae OS loss was almost complete, whereas in CRISPR-VQR treated retinae the OS layer was still present although strongly reduced in length (**Fig. 4E-Q**). Thus also at 3 months of age our treatment preserved ONL and OS length from the damage induced by the $Rho^{+/P23H}$ mutation, despite worsening caused by the electroporation procedure. Additional immunohistochemical characterization of the phenotypic rescue at 1 and 3 month was performed in order to define more rigorously: layers appearance, rhodopsin localization, presence of cones, microglia activation and astroglial reactivity (**Fig. S8**). Drastic changes were observed between 1 and 3 months old retinae in all the stainings. No Rhodopsin delocalization was detected in any condition (**Fig S8E-H**), as also expected since our mice model does not present with it (34). Differences among control and respective treatment could be detected only in ONL thickness at 3 months (as expected, **Fig S8C-D**) and in GFAP reactivity that resulted milder in treated vs. control retinae at both time points although it was present in all conditions (**Fig S8Q-T**).

To obtain a functional correlate of the morphological diversity between CRISPR-VQR and control treated photoreceptors, we performed transretinal ERG recordings in 3 months old treated mice (**Fig. 4R-T**). Clearly uninjected left retinae, presented better responses to light than the right

electroporated eyes, thus confirming an additional detrimental effect on the degenerative phenotype, caused by the electroporation procedure previously indicated by the histological analysis (**Fig. 3A-D and Fig. 4A-D**). For this reason we only compared right eye recordings upon left eye normalization (**Fig. 4U-V, see also** row data in **Table S1**). WT retinae produced robust a- and b-waves indicating functional photoreceptor- and bipolar-dependent currents. By contrast, waves recorded in control treated *Rho*$^{+/P23H}$ retinae were severely blunted consistent with the observed photoreceptor cell loss. Remarkably, *Rho*$^{+/P23H}$ retinae showed a significant rescue in both a- and b-waves indicating a functional recovery of the phototransduction visual activity (**Fig. 4**).

AAV-mediated delivery for targeting the P23H *Rho* allele in *Rho*$^{+/P23H}$ murine retinae.

AAV delivery of therapeutic gene has been proven very successful for the treatment of retinal diseases in various clinical and preclinical studies (19, 20, 22–24). Currently administration of viral particles for the treatment of retina or RPE has required direct injection in the subretinal space between the photoreceptor cell layer and the RPE and consequently their detachment. This procedure, although employed in retinal clinical practice is not devoid of risks and complications compared to administration into the vitreous chamber. Intravitreal (IV) injection is safer and commonly used for pharmacological treatments of retinal diseases such as Age-related Macular Degeneration (AMD). In recent years AAV technology has engineered a great numbers of new serotype variants with enhanced capabilities (50–52), thus making targeting of the retina using IV administration possible in the adult mice. The 7m8 serotype is an AAV2 variant generated for this purpose (51) and therefore it was the first one we tested for delivery in Rho$^{+/P23H}$ eyes. With a GFP expressing AAV2-7m8 (10^{12} vg/ml, 1µl/eye) the overall transduction appeared limited with an evident preference for amacrine and ganglion cells (**Fig. S9A-F**). However, the use of the human *RHO* promoter (hRHOp) to drive GFP expression did greatly improved photoreceptor transduction (**Fig. S8G**). Therefore 2 different AAV vectors were devised: one carrying an inducible Cas9-VQR and the other carrying the sgRNAmMUT together with the GFP reporter and rtTA transactivator under the control of the hRHOp (53). Since The TetO promoter requires the rtTA transactivator and doxycycline in order to be activated this system allows us to restrict Cas9 expression to rod photoreceptors. In order to ensure continuous Cas9-VQR expression, doxycycline (2mg/ml) was administered orally to mice since the day of IV injection and for all the duration of the experiment. Due to technical limits in performing IV injections delivery was performed at 3 weeks of age. Two weeks after injection of the two viruses, we tested treated and untreated retinae for the presence of indel, using T7EI assay in the P23H and WT allele (**Fig. S9H**). Unfortunately, gene editing molecular events were undetectable in these samples. The employment of two vectors for this

strategy implies that very high level of transduction need to be achieved in order to have detectable gene targeting. The 7m8 could not reach this level of targeting at least with the titer employed. More recently others and we demonstrated the high transduction efficiency in neural tissues of the new synthetic capside variant AAV9-PHP.B (50, 54). This virus was developed by a targeted modification of the AAV9 capside in order to potentiate its ability to cross the brain-blood-barrier and infect wide areas in the neuraxis (50). Given its excellent potential for therapeutic gene delivery, we tested its ability to target the retina using IV administration (**Fig. 5A)**. Great gene delivery in the whole retina and in the RPE was detectable using an AAV9-PHP.B equipped with the CBA-GFP vector cassette (**Fig. 5B-E**). All retinal cellular subtypes were targeted, but with different extent. Transduction was higher in rod photoreceptors (70 ± 5%) and amacrine cells (81 ± 7%) and lower in cone photoreceptor (45 ± 3%), ganglion (32 ± 2%), bipolar (15 ± 1%), horizontal (33 ± 2%) and Müller Glia cells (18 ± 1%) (**Fig. 5F-M**). These findings prompted us to use the AAV-PHP.B variant to treat $Rho^{+/P23H}$ retinae with our CRISPR/spCas9-VQR approach, by delivering the two different constructs described above (**Fig. 6A**). GFP transduction carried by the vectors was robust and diffuse in the ONL of the whole retina (**Fig. 6B**). Consequently, we were able to evaluate indel frequency exclusively into rod photoreceptors, after FACS sorting for GFP+ cells. The P23H *Rho* allele of these retinae presented a significant, but moderate levels of cleavage (9.6 ± 0.4, n=3) (**Fig. 6C**). On the contrary, the WT *Rho* allele remained completely unaltered in all the treated retinae (**Fig. 6D**). Unfortunately, indel quantification in these samples was hampered by the low sensitivity with both the TIDE (**Fig. 6H**) and the clonal analysis (data not shown). In order to solve this problem, we investigated the possibility of enriching for the editing events separating the cells with high and low levels of GFP transduction (GFP-high and GFP-low respectively) by FACS sorting (**Fig. 6E**). Indeed, the GFP-high, respect to the GFP-low, population exhibited a much higher accumulation of indels (**Fig. 6F**), as measured by T7EI assay at the level of the P23H *Rho* allele. Once more, the WT *Rho* allele instead was not affected (**Fig. 6G**). Interestingly, TIDE analysis revealed an 15 fold difference in indel efficiency between the parental GFP^+ (**Fig. 6H**) and GFP-high population (**Fig. 6I**). This increment in indel mutation allowed for indel frequency analysis in retinal samples revealing that in viral transduced retinae as much as in electroporated retinae the most present indel by far is the insertion of a single nucleotide (**Fig. 6I**). Furthermore GFP+ and GFP-high samples were subjected to NGS analysis to refine indel analysis and compare them with GFP+ sorted samples of electroporated retinae (**Fig. 7A**).

NGS analysis of edited $Rho^{+/P23H}$ murine retinae

For sequencing analysis we devised a PCR that unselectively amplified both WT and P23H *Rho*

allele, in order to concurrently assess their incidence and NHEJ events. Quantification of editing frequency in retinal samples was obtained using the CRISPResso toolbox (55). This analysis confirmed selectivity of our approach for the P23H *Rho* allele. In fact, WT *Rho* allele frequency in control untreated retina was comparable to treated samples, regardless of the delivery system employed or enrichment of editing events (**Fig. 7B**). Conversely, these two parameters strongly affected unedited P23H *Rho* allele frequency, that was lowest in electroporated retinae (less than 10%) compared to AAV9-PHP.B-injected retinae (38%). NHEJ events occurred in a complementary fashion in these samples (43% and 7% respectively). Indel enrichment in the GFP-high compared to the GFP+ was evident as previously assessed (**Fig. 7B**). Regardless of indel enrichment or delivery system, retinal treatments showed very similar pattern of frameshift and in-frame indel mutation (**Fig. 7C, Fig. S10 and S11**). Since both +1 and +2 frameshift mutation in the P23H *Rho* allele cause the formation of premature termination codon (**Fig 2B**), the occurrence of this type of mutation is most likely to disrupt its proteic expression and its dominant-positive detrimental effect, compared to in-frame mutations. Thus, our editing strategy revealed not only high selectivity but also robust functional silencing efficiency of the disease allele.

Selective targeting of the human WT and P23H *RHO* gene alleles

Since efficacy of the CRISPR/spCas9-VQR system was proved in a murine model of the disease and since the sgRNA-mMUT PAM site is conserved in human genome (**Fig. S1**), we sought to test this approach in a convenient human cellular model. Thus, we generated two sgRNAs based on the conserved PAM site, one targeting the WT (sgRNA-hWT) and the other the P23H mutant sequence (sgRNA-hMUT) (**Fig. 8A**). To generate a cellular model with the P23H homozygote mutation in the *RHO* gene, we devised a CRISPR/Cas9-based gene-editing approach to introduce the c.68C>A nucleotide transversion into 293T cells (**Fig. S12**). WT or gene edited $RHO^{P23H/P23H}$ 293T cells were treated with sgRNA-hWT and -hMUT and subjected to our panel of genomic cleavage assays (**Fig. 8B-U**). In all assays, both guides showed significantly different cleavage efficiency when targeting the complementary genome, compared to the one bearing one mismatch. In particular, T7EI assay quantified the sgRNA-hWT indel rate in WT cells in 60 ± 13% compared to none in P23H cells (n=3), whereas sgRNA-hMUT indel rate was down to zero in WT but up to 58 ± 14% in mutant cells (n=3). For the same conditions TIDE analysis concordantly measured cleavage efficiency in 78 ± 9%, 7 ± 1%, 3 ± 1%, 76 ±1 0% respectively (n=3). Selectivity of cleavage based on clone sequencing was even higher with 94% (in WT cells) vs 0% (in P23H cells) for the sgRNA-hWT and 89% (in p23H cells) vs 0% (in WT cells) sgRNA-hMUT. Conveniently, the fraction of indel in-frame mutation in the *RHO* coding sequence was very low for both human guides (similarly to

sgRNAmMUT) supporting the idea that this system would efficiently inactivate the pathogenic product of the P23H *RHO* mutant allele also in human retina.

Discussion

Here we exploited the efficiency of the CRISPR/Cas9 technology to selectively target a single point mutation in the genome, generating the dominant gain-of-function mutant *RHO* allele, responsible for photoreceptor cell loss and RP. Our results provide strong evidence that this approach can lead to efficient targeting of the mutant sequence and, thus, preventing the pathogenic effects of the dominant mutation, while simultaneously preserving the WT *Rho* allele. Notably, we showed that targeting specificity of sgRNAs can be strongly influenced by the seed sequence up to discriminating between two sequences which differ for a single nucleotide only. This is an invaluable finding which discloses a wide use of this approach to distinguish between two or more homologous sequences.

Surprisingly, this high level of precision and efficiency in sequence-specific targeting of the designed CRISPR elements was maintained, and even increased, after local delivery in the retinal cells, indicating that this approach maintains its specificity upon *in vivo* delivery. Such efficient targeting of the mutant *Rho* allele triggered an evident delay of the degenerative retinal process and a rescue of the retina functional activity. Since the PAM genomic site is conserved between humans and mice, we were able to prove efficacy and selectivity of this gene targeting system in human cells engineered with the P23H *RHO* gene mutation.

Previous studies have attempted to use shRNA (30) or ribozyme-based (31, 32) approaches to silence the P23H *Rho* mutant allele. In these and other studies selectivity toward the P23H Rho allele is achieved using trangenic mice or rats overexpressing the mutated P23H allele from a different species (human or rodent). In this scenario the silencing of the toxic P23H, although beneficial, can not accurately model the bi-allelic composition of the human pathology, as our knock-in mice model provides. This mouse model combined with our strategy to target selectively the mutated allele, faithfully model the disease genetic features and its potential rescue, suggesting a substantial higher therapeutic potential (30–32, 56). Indeed Rhodopsin selective inactivation by the CRISPR/Cas9 system has been recently proved possible in transgenic rats carrying a murine mutant allele (57). In this study sgRNA selectivity relied mainly on species-specific and not allelic differences. Moreover S334X dominant *Rho* allele targeted in this study is not conserved in humans and, thereby, not relevant for human disease pathology. Hence this approach provided a proof-of-principle of feasibility but is not suitable for translation into human therapy. Beyond the

CRISPR/Cas9-mediated editing, other approaches have been attempted for the attenuation of dominant *Rho* alleles causing RP. Albeit some therapeutic benefit was achieved, the repression of the mutant allele resulted not complete and its effect was weakened with time *in vivo* providing relevant obstacles for any clinical development. In this regard, our approach has the strong advantage to produce a stable and definitive genetic change in the targeted cells even with a single application. An interesting therapeutic option is the suppression and replacement (31, 33, 53) approach based on the silencing of both WT and mutant *RHO* alleles, while simultaneously adding an extra functional copy of the gene resistant to silencing. Nonetheless, the drawback of this approach is that RHO ectopic expression, ensured by current gene transfer tools, can not meet its endogenous levels, necessary for recovery.

Various mutations in the *RHO* gene have been identified to cause adRP. Currently, despite the *Rho* c.68C>A mutant allele is by far the most common mutation in north America, more than other 90 mutations have been identified in the *RHO* gene responsible for adRP and congenital stationary night blindness (https://sph.uth.edu/retnet/). Remarkably, we identified PAM domains from different Cas9 ortholog (26, 27, 58) or their variants overlapping or in close proximity (< 4 bases distant) within a large set of these disease-causing mutations (**Fig. S13).** More in general, this methodology can have application to the dominant retinal dystrophies caused by mutations in the *IMPDH1* (59), *PRPF3* (6, 8) and *KLHL7* (60) genes.

Overall AAVs are considered the tool-of-choice for therapeutic gene delivery in the retina. Moreover the development of different capsid serotypes and novel variants have been instrumental for an efficient targeting of different cell populations within the retina using subretinal injections. Nonetheless, very recent studies have shown that this administration route might lead to some moderate systemic inflammation that might worsen the overall pathological state (21, 22). On this regard, intravitreal administration of AAVs has potentially a much safer profile, but has often resulted in a significant reduction of retinal transduction especially for photoreceptor cells, that are the cellular target for a predominant number of retinal diseases. However the viral vector toolbox available for retinal research has recently been remarkably expanded with the discovery of new and potent AAV variants. In this work we demonstrated, for the first time, the great potential of the AAV.PHP-B synthetic variant for intravitreal delivery of gene therapeutics to target the retinal photoreceptor cells. Importantly, the use of this vector allowed us to effectively deliver the CRISPR/Cas9-VQR system into the whole retina. Inactivation of the P23H *RHO* allele by the AAV.PHP-B-delivered CRISPR/Cas9-VQR system was proven specific and effective, but it was restricted to only a small fraction of photoreceptor cells (about 10%). A critical aspect limiting the success of the present approach is the need of using more than one AAV to deliver all the necessary

CRISPR elements. In fact, although, AAV-mediated SpCas9 genome editing *in vivo* has already been proved (61), its delivery cannot be performed in a single particle. This drawback was recently overcome by the identification of the new SaCas9 ortholog sufficiently small to be packaged in an AAV vector with its sgRNA (26). The use of this system enabled a strategy to edit the *distrophin* mutant gene *in vivo* as a new therapeutic opportunity for treating Duchenne muscular dystrophy (35, 36). Moreover a new variant, SaCas9-KHH, was engineered to broaden its genome targeting range. Nonetheless, the two different sgRNAs for this Cas9, that would selectively target the P23H allele, exhibited a very poor cleavage efficiency in our experimental setting. Thus, more work is needed to broad the effective potential, and predict the favorable targeting events for the SaCas9 and its derivatives.

Overall, we believe that, this particular approach to be therapeutically valuable necessitates of an convenient and efficient delivery of the CRISPR components to the relevant tissue and cells and that IV administration of the PHP-B variant meets these need.

Notably, this is the first time that a Cas9 variant has been exploited to reach allele specific targeting. More broadly this study represents a convincing proof-of-concept for wide application of the CRISPR system for dominant genetic human disorders, caused by mutant gain-of-function or dominant-negative gene alleles. The broad applicability of this approach depends on the identification of new bacterial Cas9 orthologs, and their engineered variants with intact nuclease activity. Recently this pool has strongly expanded the targeting range of this system providing a significant flexibility for genome-wide engineering (Cong et al., 2013; Kleinstiver et al., 2015; Zetsche et al., 2015).

The employment of the gene editing methods always raises safety concerns about off-target effects, especially when translational applications are taken into consideration. We did not observe off-target mutations at potential off-target sites in the mouse genome nor any evident long-term abnormalities in retinae after electroporation. However, off-target mutations may occur at sites beyond those predicted in silico, hence a comprehensive and unbiased analysis, such as whole genome sequencing, would be an essential component of future efforts to definitively establish the safety of this approach (26, 62–64). Various approaches have been conceived in order to restrict Cas9 activity in time and reduce its detrimental off-target effects (65, 66). In our system the use of TetO promoter to induce Cas9 could be useful control its expression with doxycycline and identify a therapeutic window in which Cas9 therapeutic action is deprived of undesired effect. Moreover this system might me implemental in order to clarify when during disease progression our approach is effective since as the disease progress it is less likely that gene correction can revert RP symptoms.

These results provide strong evidence that the CRISPR/Cas9 system can be tailored to target the mutant *Rho* allele, restoring retinal function, thus opening new strategies for human dominant genetic disorders, in particular afflicting the eye. Moreover this approach was successfully combined with IV delivery using the AAV-PHP.B variant, thus reinforcing its translational potential.

Materials and Methods

Vectors generation

The oligo (Sigma-Aldrich) pairs encoding the 20-nt guide sequences and including overhangs for ligation into the BsmbI site (Oligos List) were annealed and ligated (Clontech) into the LV-U6-filler-gRNA scaffold plasmid previously linearized with the BsmBI restriction site, thus removing the filler sequence. This vector was engineered replacing the TetO-NfiA cassette of the TetO-FUW-NfiA plasmid (67) (Addgene) with the 'U6-promoter-filler-gRNA scaffold' of the LentiCRISPR (38) (Addgene). In order to provide the LV-U6-filler-gRNA scaffold vectors with a selection, a Blast cassette under the Ef1a core promoter was cloned downstream of the U6-sgRNA cassette. Moreover this vector was further modified replacing the gRNA scaffold optimized for spCas9 with an other contained in the vector p.X601 (26) (Addgene) selective for saCas9. Replacing the Nfia cassette of the TetO-FUW-NfiA with the spCas9-p2aPuro sequence of LentiCRISPR we obtained the TetO-spCas9-p2a-Puro vector, from which the TetO-SaCas9-KHH-p2a-Puro vector was derived (taking advantage of MSP2292, Addgene). The plasmid pCAG-spCas9-VQR was generated from the pCAG-spCas9 (cloned by replacing GFP of the pCAG-GFP (42), Addgene, with spCas9 of the LentiCRISPR) vector by overlap-extension PCR (Phusion® High Fidelity DNA Polymerase, New England Biolabs, NEB) using appropriate primers (Oligos List) to modify codon 1135 (GAC into GTG), 1335 (AGG into CAG) and 1337 (AAC into AGA) of the native spCas9, thus producing the VQR variant. The same strategy was used for the generation the TetO-spCas9-VQR-p2a-Puro vector.

Similarly we constructed an inducible adenoviral vector containing the spCas9-VQR form the pX551 vector (Addgene), which was further modified replacing the Mecp promoter with the TetO promoter. A second adenoviral vector was generated using an AAV2-hRHO-promoter-GFP vector (kindly donated by Dr. A. Auricchio) introducing the U6-sgRNAmMut cassette upstream of the hRHO promoter and a GFP-t2a-rtTA cassette downstream.

Wild-type Rho CDS sequence was amplified from whole cDNA derived from retrotranscription (iScript cDNA synthesis kit, Bio-Rad) of RNA extracted (TRIzol® Reagent, Thermo Fisher Scientific) from adult retinae. The oligos employed for this purpose (Rho-EcoRI-AgeI-koz-Fw and Rho-NheI-EcoRI-R, Oligos List) allowed for direct cloning into the pCAG-ires-GFP plasmid using EcoRI, but also further subcloning in to the pCAG vector using EcoRI-NheI restriction sites. The N-terminus of the mRho wild-type sequence was substituted with the corresponding region of the other variants (P23H, IndelA e IndelB) using PCR almplification (oligos: Rho-EcoRI-AgeI-koz-Fw and Rho-Xho-RI, Oligos List) and AgeI and XhoI restriction site from molecular cloning.

Cell cultures

MEFs were isolated from E14.5 $Rho^{P23/P23H}$, $Rho^{P23/+}$ and $Rho^{+/+}$ mice embryos. Primary culture were derived as previously described (67) and maintained in MEF medium (Dulbecco's Modified Eagle Medium, containing 10% fetal bovine serum, non-essential amino acids, sodium pyruvate and penicillin/streptomycin, Thermofisher Scientific). 293T cells were cultured in the MEFs media, whereas P19 cell lines were maintained in α-MEM (Sigma-Aldrich) supplemented with 10% FBS. Cells were split every 3-4 days using Trypsin (Sigma-Aldrich) dissociation (0.25%) in their medium. MEFs or 293T cells were infected (0,5µL of $\approx 10^{+8}$ titer for 50,000 cells) in MEF medium containing doxycycline (2µg/ml, Sigma). 16–20 h after infection cells were switched into fresh MEF media containing doxycycline and puromycin (1µg/ml, Sigma) and blastidicin (10 µg/ml, ThermoFisher Scientific), unless specified otherwise. 48-72 h after cells were harvested for further analysis. P19 and 293T cells were transfected with lipofectamine/PLUS reagent (ThermoFisher Scientific) according to manufacturer instruction. Upon transfection with spCas9 and sghRHO-REC constructs and ssODN, 293T cells were selected for 48h with puromycin (1µg/ml, Sigma), and blastidicin followed by single cell FACS-sorting into a 96well plate.

Viral production

Lentiviral replication-incompetent, VSVg-coated lentiviral particles were packaged in 293T cells (68). AAV replication-incompetent, recombinant viral particles were produced in 293T cells by polyethylenimine (PEI, Polyscience) co-transfection of three different plasmids: transgene-containing plasmid, packaging plasmid for rep and cap genes and pAdDeltaF6 for the three adenoviral helper genes. The cells and supernatant were harvested at 120 hrs. Cells were lysed in Tris buffer (50mM Tris pH=8,5, 150mM NaCl, Sigma-Aldrich) by repetitive freeze-thawing cycles (3 times). In order to clarify the lysate Benzonase treatment was performed (250U/mL, 37°C for 30min, Sigma-Aldrich) in presence of 1mM $MgCl_2$ (Sigma-Aldrich) and cellular debris separated by centrifugation (2000g, 30min). The viral particles present in the supernatant instead were concentrated by precipitation with 8% PEG8000 (Polyethylene glycol 8000, Sigma-Aldrich), resuspended in Tris buffer and combined with corresponding cell lysates. The viral phase was isolated by iodixanol step gradient (15%, 25%, 40%, 60% Optiprep, Sigma-Aldrich) in the 40% fraction and concentrated in PBS (Phosphate Buffer Saline) with 100K cut-off concentrator (Vivaspin20, Sartorius Stedim). Virus titers were determined by measuring the number of DNase I-resistant viral particles, using qPCR with linearized genome plasmid as a standard.

Animal models and manipulation

All procedures on animals were performed in accordance with the institutional guidelines for animal research. Homozygous P23H knock-in mice (obtained from The Jackson Laboratory, Bar Harbor, ME) were bred either with each other in order to maintain the homozygous line or with C57BL/6 mice (Charles River Italy, Calco, Italy) in order to obtain to generate P23H heterozygous embryos and pups. P0 mice were electroporated as previously described (Matsuda and Cepko, 2004). Shortly they were anesthetized by chilling on ice, and a small incision was made in the eyelid and sclera near the lens with a 30-gauge needle. 0.3µl of DNA solutions (3-6 mg/ml, 0.1% fast green) were injected into the subretinal space through the incision by means a Hamilton syringe with a 33-gauge blunt-ended needle. Upon DNA injection, five square pulses of 80V amplitude and 50ms duration (with 950 ms intervals) were applied to the heads of the pup using tweezer-type electrodes (model 520, 7 mm diameter, BTX, San Diego), connected to a pulse generator ECM830 (BTX). DNA was transfected only into right eyes. Left eyes were left untouched. Upon 4-12 weeks retinae were harvested for indel analysis, histological staining or ERG recordings. For AAV invtravitreal (IV) injections, 3/4-week-old mice were anaesthetized with an intraperitoneal injection of ketamine (80 mg/kg; Ketavet 100 - Intervet Productions s.r.l., Aprilia IT) and xylazine (10 mg/kg; Rompun® - Bayer s.p.a., Milano, IT). 1 µL of AAV-CBA-GFP ($1x10^{12}$ viral genomes/mL, vg/mL) or of a 1:1 mixture of AAV-Cas9-VQR ($1x10^{12}$ vg/mL) and AAV-U6sgRNAmMUT-RHOp-GFP-t2a-rtTA ($1x10^{12}$ vg/mL) was intravitreally injected using a Hamilton syringe with a 33-gauge blunt-ended needle under a stereo microscope (Leica Microsystems Ltd.). Doxicycline (2mg/mL) was administered in the drinking water from the day of injection till retinal harvest. 2 weeks after injection retinae were harvested for subsequent analysis.

Tissue and cell collection

Electoporated retinae were dissected under a fluorescence dissecting microscope. GFP^+ retinae were selected for further analysis based on fluorescence intensity and diffusion, but also retinal integrity. In order to perform immunohistochmical analysis dissected retinae were fixed with 4% paraformaldehyde in PBS for 20 min at room temperature, cryoprotected in 5% sucrose (10min) followed by 30% sucrose (10 min), and embedded in OCT compound on dry ice. Cryostat cryosections (20 µm) were then cut. In case of indel analysis retinae were dissociated (papain 10U/mL, Worthington, 10min, 37°C) (69) and FACS-sorted (MoFlo, Beckman Coulter, Inc.). Genomic DNA was extracted from the GFP^+ population thus isolated using QIAamp DNA micro kit (QIAGEN) following manufacturer instruction.

Genomic DNA (gDNA) was extracted from MEFs and 293T cells using a lysis buffer (100 mM Tris-HCl pH8, 200 mM NaCl, 5 mM EDTA, 0.5% SDS with proteinase K, Sigma-Aldrich) to

incubate cells (4-24h, 55°C). gDNA was purified using isopropanol and ethanol 70% and resuspended in water. RNA extraction was performed using Trizol®Reagent according to manufacturer instruction (TRIzol® Reagent, Thermo Fisher Scientific). For immunohistochemical analysis cells were fixed 4% paraformaldehyde.

Indel analysis and off-target analysis

The genomic regions that were flanking the sgRNAs target sites were amplified by PCR using 100 ng of genomic DNA as a template. Primers sequences for the selective or unselective amplification of both WT and P23H Rho alleles are indicated in Oligos List as well as primers for hRHO amplification. Selective Rho^{+} and Rho^{P23H} PCR required an annealing temperature of 66°C and 68°C respectively while 62°C was routinely used as annealing temperature for unselective PCRs. For T7EI analysis, 200 ng of purified PCR products (Wizard SV gel and PCR Clean-Up System, Promega) were denatured and reannealed in NEB buffer 2 (New England Biolabs): 95°C, 5 min; 95°C-85°C at -2°C/s; 85°C-25°C at -0.1°C/s. Upon reanneling 10U of T7EI (New England Biolabs) were added and incubated at 37°C for 15 min to then be analysed on 2% agarose gels, imaged with a Gel Doc gel imaging system (Bio-Rad). The percentage of genome modification was obtained as previously described (25). To perform TIDE assay, purified PCR products were analyzed by Sanger sequencing (GATC Biotech). The quantification of genome modification was also obtained using the TIDE software, which allowed to interpolate the chromatograms produced by direct Sanger sequencing of the previously described PCR products or which applies a deconvolution algorithm on the sequencing traces to identify the indel mutations proximal to the editing site and accurately determines their frequency in a cell population(37). Sequencing primers used for TIDE analysis are indicated in Oligos List. Amplicons obtained as above were also subjected to clone sequencings, which consisted in cloning of PCR products using the TOPO BLUNT cloning kit following manufacturer instruction (ThermoFisher Scientific) and then select and individually sequence clones positive for the amplicon of interest. RFLP (Restiction Fragment Length Polymorphism) analysis was also carried out either on amplicons (293T selection for recombined clones with BstBI) or individual clones (optimization of PCR selectivity, BanII). Briefly 2-500 ng of DNA were incubated with 5U of BanII or BstBI (NEB) at for 2 at 37°C or 65°C respectively to then be analysed on 2% agarose gels. Off-target were identified Using COSMID on-line tool(41) (https://crispr.bme.gatech.edu) and assayed by PCR amplification (see Oligos List), to be tested both by TIDE analysis and clone sequencings.

NGS Analysis

PCR amplicons were analyzed by NGS performed by CTGB core Facility at Ospedale San Raffaele (Milan, Italy). Genomic PCR products were subjected to library preparation using the NEBNext Ultra II DNA library Kit (NEB). Briefly, common primers are added by ligation, following by limited number of PCR cycles (eight cycles) where specific barcode for each sample was added. Amplicones were purificated with AMPure beads (Beckman Coulter) and run onto Bioanalyzer 2100 (Agilent). Equimolar amounts of library were mixed, diluited and sequenced with an Illumina MiSeq system. CASAVA software (Illumina) was used for demultiplexing. Fastq reads were aligned to the mm10 reference genome with Bowtie (70). NHEJ as well as frameshift/inframe mutations were quantified with CRISPResso (55).

List of primers

Oligos for overlap-extension PCR

VQR-SacI-FE GAGCTCGTGAAAGTGATGGGCCGGCAC

VQR-FI1 GACCCTAAGAAGTACGGCGGCTTCGTGAGCCCCACCGTGGCCTATTCTG

VQR-RI1 CAGAATAGGCCACGGTGGGGCTCACGAAGCCGCCGTACTTCTTAGGGTC

VQR-FI2 CACCACCATCGACCGGAAGCAGTACAGAAGCACCAAAGAGGTGCTGGAC

VQR-RI2 GTCCAGCACCTCTTTGGTGCTTCTGTACTGCTTCCGGTCGATGGTGGTG

VQR-NheI-RE CGCCGCTGCCGCTAGCTTTCTTTTTCTTAGC

Oligos for molecular cloning

Rho-EcoRI-AgeI-koz-Fw CCGGAATTCACCGGTGGCACCATGAACGGCACAGAGGGCCC

Rho-NheI-EcoRI-R CCGGAATTCGCTAGCTTAGGCTGGAGCCACCTGGC

Rho-Xho-RI GCCCTCGAGATTACAGCCTGTGGG

sgRNA Oligo pairs

sgRNA-saC1 Fw:caccgCCAGGTAGTACTGCGGCTGCT; Rv:aaacAGCAGCCGCAGTACTACCTGGc

sgRNA-saC2 Fw:caccgACTGCGGCTGCTCGAAGTGGC; Rv:aaacGCCACTTCGAGCAGCCGCAGTc

sgRNA-hEMX1 Fw:caccgGGCCTCCCCAAAGCCTGGCCA; Rv:aaacTGGCCAGGCTTTGGGGAGGCCc

sgRNA-US Fw:caccgGGTTCCGCCAGGTAGTACTG; Rv:aaacCAGTACTACCTGGCGGAACCc

sgRNA-mMUT Fw:caccgGGCGTGGTGCGGAGCCACTT; Rv:aaacAAGTGGCTCCGCACCACGCCc

sgRNA-mWT Fw:caccgGGCGTGGTGCGGAGCCCCTT; Rv:aaacAAGGGGCTCCGCACCACGCCc

sgRNA-REC Fw:caccgTAGTACTGTGGGTACTCGAA; Rv:aaacTTCGAGTACCCACAGTACTAc

sgRNA-hWT Fw:caccgGGTGTGGTACGCAGCCCCTT; Rv:aaacAAGGGGCTGCGTACCACACCc

sgRNA-hMUT Fw:caccgGGTGTGGTACGCAGCCACTT; Rv:aaacAAGTGGCTGCGTACCACACCc

Oligos for cleavage analysis	Amplicon size (nt)	
mRho (unspec)	Fw:CCAGGTCCCTGGTCATCTTCTC; Rv:TCTGAACCCATGTTTCTTGC	amplicon: 1520nt
hEMX1	Fw:GGAGCAGCTGGTCAGAGGG; Rv:CCATAGGGAAGGGGGACACTGG	amplicon: 690nt
PCR-WT	Fw:GCAGTGGGATTAGCGTTAG; Rv:TCTGAACCCATGTTTCTTGC	amplicon: 790nt
PCR-P23H	Fw:CAGCAGTGGGATTAGCGTACC; Rv:TCTGAACCCATGTTTCTTGC	amplicon: 790nt
hRHO	Fw:TCAGGCTTCCTCCTAGTGTC; Rv:GGCTTCCAACTCAACTCTGC	amplicon: 960nt

Oligos for Off-target analysis

1600002D24Rik	Fw:CCTTGTGCCATGAACCTTT; Rv: GGAGCAAGCCAACCTTGTAT	amplicon: 790nt
Irf5	Fw:GCACAGCAAACAGGTAGGTC; Rv: ACACTTTCCCTTCACGTTCA	amplicon: 710nt
Arrb2	Fw:GGCCCTCAGAACTAGACAGC; Rv: CGCTCCACTCCAATATCTCA	amplicon: 700nt
Rp9	Fw:TTCCATTTGGTTGTGGTGTT; Rv: TGAAAGGGTAACAGCGTCAG	amplicon: 670nt
Oligos for clone sequencing		
mRho-seq-Fw	CTCGCGGATGCTGAATCAGC	
hEMX1-Rv	CCATAGGGAAGGGGGACACTGG	
hRHO-seq-Fw	CTCCCAGATGCTGATTCAGCC	

Histological analysis and morphological measurements.

Retinal sections and fixed cells were permeabilized for 30 min in blocking solution, containing 0.2% Triton X-100 (Sigma) and 10% donkey serum (Sigma), and incubated overnight at 4°C with the primary antibodies in blocking solution. Primary antibodies were used: rabbit-anti calnexin (Sigma-Aldrich, 1:500), mouse anti-CNGA (kindly provided by Dr Molday, 1:20) chicken anti-Green Fluorescent protein (ThermoFisher Scientific, 1:2000) mouse anti-Rhodopsin (Sigma-Aldrich, 1:1000), rabbit anti-Rhodopsin (Abcam, 1:500), rabbit anti-Red-Green-Opsin (Millipore, 1:500), rabbit anti-GFAP (Dako, 1:500), rabbit Iba (Wako, 1:500). Upon wash with PBS (3x) slides were incubated for 1h at RT in blocking solution with Hoechst and secondary anibodies mix: 488Alexa-conjugated anti-chicken coupled with either Alexa Fluor-594 and Alexa Fluor-647 anti-rabbit or anti-mouse secondary antibodies (1:1000, ThermoFisher Scientific). After PBS washes (3x) slides were mounted. Confocal images were captured with Leica TCS SP5 Laser Scanning Confocal microscope (Leica Microsystems Ltd.). Confocal images were used to evaluate outer nuclear layer (ONL) thickness, a surrogate for photoreceptor number (43) and OS thickness (31). Quantification were made by measuring 10 electroporated positions (identified by GFP expression) evenly spaced 1 mm apart from the optic nerve (5 superior loci and 5 inferior loci) under 63 magnification. Further digital 3 magnification was utilized for OS thickness measurements. The CNGA and CNX stainings were utilized in oreder to assess OS/IS boundary. Measurements were made using the Leica LAS AF Lite software and averaged between the different animals. Three eyes per electroporation condition were measured as well as controlateral eyes as non-electroporated samples (NE).

RNA analysis

Upon extraction, whole RNA (TRIzol® Reagent, Thermo Fisher Scientific) of transfected P19 cells was retrotranscribed (iScript cDNA synthesis kit). The absence pCAG plasmid contamination in whole cDNA was revealed by RT-PCR using following oligos (5′-3′): Fw, GCGGCGGCAGCCAATCAGAG, Rv, CACAAAGGGCCCTCCCGGAG and GoTaq Polymerase

(Promega). *mRho* RNA levels were measured using quantitative real time PCR (qPCR) using Titan HotTaq EvaGreen qPCR mix (BioAtlas) by means of a C1000 Thermal Cycler (Biorad). *18S* mRNA levels were used as normalizer. Primers for *Rho* were (5′-3′): Fw, ATGAGCAACTTCCGCTTCG, Rv, ATGAGCAACTTCCGCTTCG. Primers for *18S* were: Fw, GTAACCCGTTGAACCCCATT, Rv, CCATCCAATCGGTAGTAGCG. cDNA was also tested for different *Xbp1* isoform by RT-PCR as already described (47). *Xbp1* expression was also tested by an *XBP1* reporter plasmid (71) (kindly provided by Dr. M. D'antonio) co-transfected into p19 cells in combination with different Rhodopsin variants. In this case *XBP1* splicing was evaluated by GFP fluorescence intensity as evaluated by FACS-sorting.

ERG

Scotopic electroretinogram (ERG) responses were evaluated in WT, Cas9 VQR only and Cas9 VQR + Sg RNA mMUT mice at 3 months of age. Mice were dark-adapted for 2 (72) hours before the recordings and all procedures were conducted under dim-red light. Briefly, mice were anesthetized with an intraperitoneal injection of ketamine (80 mg/kg; Ketavet 100 - Intervet Productions s.r.l., Aprilia IT) and xylazine (10 mg/kg; Rompun® - Bayer s.p.a., Milano, IT). Pupils were dilated with 0.5% Tropicamide (Visumidriatic - Visufarma s.p.a., Roma, IT) and 2% Hydroxypropylmethylcellulose (GEL 4000 - Bruschettini s.r.l., Genova, IT) was applied to avoid eye drying. Body temperature was maintained with a homeothermic pad at 37°C (Harvard Apparatus, Holliston MA, US). ERG was recorded using corneal ERG electrodes (73) connected via flexible cables to a Micromed amplifier (SystemPlus Evolution - Micromed s.p.a., Mogliano Veneto, IT). Data were acquired at a sampling frequency of 4096 Hz, coded with 16 bits and filtered between 5-70 Hz. Flash stimuli, with intensity of 231 mJ and duration of 10 μs, were delivered to both eyes at a frequency of 0,5 Hz with a Flash10s photo stimulator (Micromed s.p.a., Mogliano Veneto, IT) placed 15 cm from the eyes. For each session, 6 averages of 10 trains each were used for measuring the amplitude of a-wave (baseline to negative a-wave peak) and b-wave (a-wave peak to positive b-wave peak). a-wave and b-wave amplitudes were normalized on the ERG recorded from the non-electroporated LE of the same mouse. $Rho^{P23H/+}$ mice electroporated at P0 as above were recorded at 1 month of age. Normalized ERG amplitudes were analyzed using one-way ANOVA (three mice strains at one time point) followed by LSD post-hoc test.

Quantifications and statistical analysis

To the exception electrophysiological measurements (see above) expression or indel data are represented as the mean of biological replicates and the variation as standard standard deviation

(SD). For each experiment, "n" indicates the number of independent cultures used. Statistical significance of differences between control and target data sets was determined with one-way ANOVA and post-hoc analysis (Graph Pad Prism); differences with $P \leq 0.05$ were considered statistically significant.

Author contributions

S.G.G. and V.B. conceived and planned the experiments; S.G.G. performed the experiments and analyzed data; M.L. contributed in gene cloning, sequencing and lentiviral particles production; L.M. and T.C. processed and stained isolated mouse retinae; A.D. and M.A. carried out and elaborated the Sanger sequencing data; V.C., G.D. and L.L. performed and analyzed the ERG recordings; V.B. supervised and supported the project and wrote the paper together with S.G.G.

Acknowledgments

We thank Dr. A. Lombardo, K. Joung, V. Marigo, A. Recchia, E. Van Anken, M. D'Antonio and V. Ranganathan for helpful discussion and sharing of reagents. We are thankful to the FRACTAL core facility for expert supervision in flow-cytometry. This work was supported by the European Research Council (AdERC #340527) and Fondazione Roma.

Conflict of Interest Statement

No competing financial interests are linked directly or indirectly to this study.

References

1. Hamel, C. (2006) Retinitis pigmentosa. *Orphanet J. Rare Dis.*, **1**, 40.
2. Kennan, A., Aherne, A. and Humphries, P. (2005) Light in retinitis pigmentosa. *Trends Genet.*, **21**, 103–110.
3. Daiger, S.P., Bowne, S.J. and Sullivan, L.S. (2007) Perspective on Genes and Mutations Causing Retinitis Pigmentosa Stephen. *Arch. Ophthalmol.*, **125**, 151–158.
4. Wang, D.Y., Chan, W.M., Tam, P.O.S., Baum, L., Lam, D.S.C., Chong, K.K.L., Fan, B.J. and Pang, C.P. (2005) Gene mutations in retinitis pigmentosa and their clinical implications. *Clin. Chim. Acta.*, **351**, 5–16.
5. Ayuso, C., Garcia-Sandoval, B., Najera, C., Valverde, D., Carballo, M. and Antinolo, G. (1995) Retinitis pigmentosa in Spain. The Spanish Multicentric and Multidisciplinary Group for Research into Retinitis Pigmentosa. *Clin Genet*, **48**, 120–122.
6. Sullivan, L.S., Bowne, S.J., Birch, D.G., Hughbanks-Wheaton, D., Heckenlively, J.R., Lewis, R.A., Garcia, C.A., Ruiz, R.S., Blanton, S.H., Northrup, H., *et al.* (2006) Prevalence of disease-causing mutations in families with autosomal dominant retinitis pigmentosa: A screen of known genes in 200 families. *Investig. Ophthalmol. Vis. Sci.*, **47**, 3052–3064.
7. Milla, E., Maseras, M., Martinez-Gimeno, M., Gamundi, M.J., Assaf, H., Esmerado, C. and Carballo, M. (2002) [Genetic and molecular characterization of 148 patients with autosomal dominant retinitis pigmentosa (ADRP)]. *Arch Soc Esp Oftalmol*, **77**, 481–484.
8. Ziviello, C., Simonelli, F., Testa, F., Anastasi, M., Marzoli, S.B., Falsini, B., Ghiglione, D., Macaluso, C., Manitto, M.P., Garrè, C., *et al.* (2005) Molecular genetics of autosomal dominant retinitis pigmentosa (ADRP): a comprehensive study of 43 Italian families. *J. Med. Genet.*, **42**, e47.
9. Tee, J.J.L., Smith, A.J., Hardcastle, A.J. and Michaelides, M. (2016) RPGR-associated retinopathy: clinical features, molecular genetics, animal models and therapeutic options. *Br. J. Ophthalmol.*, **100**, 1022–1027.
10. Iannaccone, A., Man, D., Waseem, N., Jennings, B.J., Ganapathiraju, M., Gallaher, K., Reese, E., Bhattacharya, S.S. and Klein-seetharaman, J. (2006) Retinitis pigmentosa associated with rhodopsin mutations : Correlation between phenotypic variability and molecular effects. **46**, 4556–4567.
11. Dryja, T.P., McGee, T.L., Hahn, L.B., Cowley, G.S., Olsson, J.E., Reichel, E., Sandberg, M.A. and Berson, E.L. (1990) Mutations within the rhodopsin gene in patients with autosomal dominant retinitis pigmentosa. *N Engl J Med*, **323**, 1302–1307.

12. Sung, C.H. and Chuang, J.Z. (2010) The cell biology of vision. *J. Cell Biol.*, **190**, 953–963.

13. Tam, B.M. and Moritz, O.L. (2006) Characterization of rhodopsin P23H-induced retinal degeneration in a Xenopus laevis model of retinitis pigmentosa. *Investig. Ophthalmol. Vis. Sci.*, **47**, 3234–3241.

14. Murray, A.R., Vuong, L., Brobst, D., Fliesler, S.J., Peachey, N.S., Gorbatyuk, M.S., Naash, M.I. and Al-Ubaidi, M.R. (2015) Glycosylation of rhodopsin is necessary for its stability and incorporation into photoreceptor outer segment discs. *Hum. Mol. Genet.*, **24**, 2709–2723.

15. Naash, M.I., Hollyfield, J.G., al-Ubaidi, M.R. and Baehr, W. (1993) Simulation of human autosomal dominant retinitis pigmentosa in transgenic mice expressing a mutated murine opsin gene. *Proc. Natl. Acad. Sci. U. S. A.*, **90**, 5499–5503.

16. Orhan, E., Dalkara, D., Neuillé, M., Lechauve, C., Michiels, C., Picaud, S., Léveillard, T., Sahel, J.A., Naash, M.I., LaVail, M.M., *et al.* (2015) Genotypic and phenotypic characterization of P23H line 1 rat model. *PLoS One*, **10**, 1–21.

17. Haeri, M. and Knox, B.E. (2012) Rhodopsin mutant P23H destabilizes rod photoreceptor disk membranes. *PLoS One*, **7**, e30101.

18. Sakami, S., Kolesnikov, A. V., Kefalov, V.J. and Palczewski, K. (2014) P23H opsin knock-in mice reveal a novel step in retinal rod disc morphogenesis. *Hum. Mol. Genet.*, **23**, 1723–1741.

19. den Hollander, A.I., Roepman, R., Koenekoop, R.K. and Cremers,F.P.M. (2008) Leber congenital amaurosis: Genes, proteins and disease mechanisms. *Prog. Retin. Eye Res.*, **27**, 391–419.

20. Bainbridge, J.W.B., Smith, A.J., Barker, S.S., Robbie, S., Henderson, R., Balaggan, K., Viswanathan, A., Holder, G.E., Stockman, A., Bhattacharya, S.S., *et al.* (2008) Effect of gene therapy on visual function in Leber's congenital amaurosis. *N Engl J Med*, **358**, 2231–2239.

21. Maguire, A.M., Simonelli, F., Pierce, E.A., Pugh, E.N., Mingozzi, F., Bennicelli, J., Banfi, S., Marshall, K.A., Testa, F., Surace, E.M., *et al.* (2008) Safety and efficacy of gene transfer for Leber's congenital amaurosis. *N. Engl. J. Med.*, **358**, 2240–2248.

22. Hauswirth, W.W., Aleman, T.S., Kaushal, S., Cideciyan, A. V, Schwartz, S.B., Wang, L., Conlon, T.J., Boye, S.L., Flotte, T.R., Byrne, B.J., *et al.* (2008) Treatment of leber congenital amaurosis due to RPE65 mutations by ocular subretinal injection of adeno-associated virus gene vector: short-term results of a phase I trial. *Hum. Gene Ther.*, **19**, 979–990.

23. Georgiadis, A., Duran, Y., Ribeiro, J., Abelleira-Hervas, L., Robbie, S.J., Sünkel-Laing, B., Fourali, S., Gonzalez-Cordero, A., Cristante, E., Michaelides, M., *et al.* (2016) Development of an optimized AAV2/5 gene therapy vector for Leber congenital amaurosis owing to defects in RPE65. *Gene Ther.*, **23**, 857-862.

24. Ali, R.R., Sarra, G.M., Stephens, C., Alwis, M.D., Bainbridge, J.W., Munro, P.M., Fauser, S., Reichel, M.B., Kinnon, C., Hunt, D.M., *et al.* (2000) Restoration of photoreceptor ultrastructure and function in retinal degeneration slow mice by gene therapy. *Nat. Genet.*, **25**, 306–310.

25. Ran, F., Hsu, P., Wright, J., Agarwala, V., Scott, D. and Zhang, F. (2013) Genome engineering using the CRISPR-Cas9 system. *Nat. Protoc.*, **8**, 2281–2308.

26. Ran, F.A., Cong, L., Yan, W.X., Scott, D.A., Gootenberg, J.S., Kriz, A.J., Zetsche, B., Shalem, O., Wu, X., Makarova, K.S., *et al.* (2015) In vivo genome editing using Staphylococcus aureus Cas9. *Nature*, **520**, 186–190.

27. Zetsche, B., Gootenberg, J.S., Abudayyeh, O.O., Slaymaker, I.M., Makarova, K.S., Essletzbichler, P., Volz, S.E., Joung, J., Van Der Oost, J., Regev, A., *et al.* (2015) Cpf1 Is a Single RNA-Guided Endonuclease of a Class 2 CRISPR-Cas System. *Cell*, **163**, 759–771.

28. Kleinstiver, B.P., Prew, M.S., Tsai, S.Q., Topkar, V.V., Nguyen, N.T., Zheng, Z., Gonzales, A.P., Li, Z., Peterson, R.T., Yeh,J.R., *et al.* (2015) Engineered CRISPR-Cas9 nucleases with altered PAM specificities. *Nature*, **523**, 481–485.

29. Lewin,A.S., Drenser,K.A., Hauswirth,W.W., Nishikawa,S., Yasumura,D., Flannery,J.G. and LaVail,M.M. (1998) Ribozyme rescue of photoreceptor cells in a transgenic rat model of autosomal dominant retinitis pigmentosa. *Nat. Med.*, **4**, 967–971.

30. LaVail, M.M., Yasumura, D., Matthes, M.T., Drenser, K.A., Flannery, J.G., Lewin, A.S. and Hauswirth, W.W. (2000) Ribozyme rescue of photoreceptor cells in P23H transgenic rats: long-term survival and late-stage therapy. *Proc. Natl. Acad. Sci. U. S. A.*, **97**, 11488–11493.

31. Mao, H., Gorbatyuk, M.S., Rossmiller, B., Hauswirth, W.W. and Lewin, A.S. (2012) Long-term rescue of retinal structure and function by rhodopsin RNA replacement with a single adeno-associated viral vector in P23H RHO transgenic mice. *Hum. Gene Ther.*, **23**, 356–366.

32. Tessitore, A., Parisi, F., Denti, M.A., Allocca, M., Di Vicino, U., Domenici, L., Bozzoni, I. and Auricchio, A. (2006) Preferential silencing of a common dominant rhodopsin mutation does not inhibit retinal degeneration in a transgenic model. *Mol. Ther.*, **14**, 692–699.

33. Mussolino, C., Sanges, D., Marrocco, E., Bonetti, C., Di Vicino, U., Marigo, V., Auricchio, A., Meroni, G. and Surace, E.M. (2011) Zinc-finger-based transcriptional repression of rhodopsin in a model of dominant retinitis pigmentosa. *EMBO Mol. Med.*, **3**, 118–128.

34. Sakami, S., Maeda, T., Bereta, G., Okano, K., Golczak, M., Sumaroka, A., Roman, A.J., Cideciyan, A.V., Jacobson, S.G. and Palczewski, K. (2011) Probing mechanisms of photoreceptor degeneration in a new mouse model of the common form of autosomal dominant retinitis pigmentosa due to P23H opsin mutations. *J. Biol. Chem.*, **286**, 10551–

10567.

35. Nelson, C.E., Hakim, C.H., Ousterout, D.G., Thakore, P.I., Moreb, E.A., Rivera, R.M.C., Madhavan, S., Pan, X., Ran, F.A., Yan, W.X., *et al.* (2016) In vivo genome editing improves muscle function in a mouse model of Duchenne muscular dystrophy. *Science*, **351**, 403–407.
36. Tabebordbar, M., Kexian, Z., Cheng, J.K.W., Chew, W.L., Widrick, J.J., Yan, W.X., Maesner, C., Wu, E.Y., Ran, F.A., Cong, L., *et al.* (2016) In vivo gene editing in dystrophic mouse muscle and muscle stem cells. *Science*, **351**, 403–407.
37. Brinkman, E.K., Chen, T., Amendola, M. and Van Steensel, B. (2014) Easy quantitative assessment of genome editing by sequence trace decomposition. *Nucleic Acids Res.*, **42**.
38. Cong, L., Ran, F.A., Cox, D., Lin, S., Barretto, R., Habib, N., Hsu, P.D., Wu, X., Jiang, W., Marraffini, L.A., *et al.* (2013) Multiplex Genome Engineering Using CRISPR/Cas System. *Science*, **339**, 819–824.
39. Hsu, P.D., Scott, D.A., Weinstein, J.A., Ran, F.A., Konermann, S., Agarwala, V., Li, Y., Fine, E.J., Wu, X., Shalem, O., *et al.* (2013) DNA targeting specificity of RNA-guided Cas9 nucleases. *Nat. Biotechnol.*, **31**, 827–32.
40. González, F., Zhu, Z., Shi, Z.D., Lelli, K., Verma, N., Li, Q.V. and Huangfu, D. (2014) An iCRISPR platform for rapid, multiplexable, and inducible genome editing in human pluripotent stem cells. *Cell Stem Cell*, **15**, 215–226.
41. Cradick, T.J., Qiu, P., Lee, C.M., Fine, E.J. and Bao, G. (2014) COSMID: A Web-based Tool for Identifying and Validating CRISPR/Cas Off-target Sites. *Mol Ther Nucleic Acids*, **3**, e214.
42. Matsuda, T. and Cepko, C.L. (2004) Electroporation and RNA interference in the rodent retina in vivo and in vitro. *Proc. Natl. Acad. Sci. U. S. A.*, **101**, 16–22.
43. Chiang, W., Kroeger, H., Sakami, S., Messah, C., Yasumura, D., Matthes, M.T., Coppinger, J.A., Palczewski, K., Lavail, M.M. and Lin, J.H. (2015) Robust Endoplasmic Reticulum-Associated Degradation of Rhodopsin Precedes Retinal Degeneration. *Mol Neurobiol.*, **52**, 679-695.
44. Illing, M.E., Rajan, R.S., Bence, N.F. and Kopito, R.R. (2002) A rhodopsin mutant linked to autosomal dominant retinitis pigmentosa is prone to aggregate and interacts with the ubiquitin proteasome system. *J. Biol. Chem.*, **277**, 34150–34160.
45. Saliba, R.S., Munro, P.M.G., Luthert, P.J. and Cheetham, M.E. (2002) The cellular fate of mutant rhodopsin: quality control, degradation and aggresome formation. *J. Cell Sci.*, **115**, 2907–2918.
46. Roman-Sanchez, R., Wensel, T.G. and Wilson, J.H. (2016) Nonsense mutations in the rhodopsin gene that give rise to mild phenotypes trigger mRNA degradation in human cells by

nonsense-mediated decay. *Exp. Eye Res.*, **145**, 444–449.

47. Jonathan, L.H., Li, H., Yasumura, D., Cohen, H.R., Zhang, C., Panning, B., Shokat, K.M., LaVail, M.M. and Walter, P. (2007) IRE1 Signaling Affects Cell Fate During the Unfolded Protein Response. *Science*, **318**, 944–949.
48. Carter-Dawson, L.D. and LaVail, M.M. (1979) Rods and cones in the mouse retina. I. Structural analysis using light and electron microscopy. *J. Comp. Neurol.*, **188**, 245–62.
49. Kennedy, B. and Malicki, J. (2009) What drives cell morphogenesis: A look inside the vertebrate photoreceptor. *Dev. Dyn.*, **238**, 2115–2138.
50. Deverman, B.E., Pravdo, P.L., Simpson, B.P., Kumar, S.R., Chan, K.Y., Banerjee, A., Wu, W.L., Yang, B., Huber, N., Pasca, S.P., *et al.* (2016) Cre-dependent selection yields AAV variants for widespread gene transfer to the adult brain. *Nat. Biotechnol.*, **34**, 204–209.
51. Dalkara, D., Byrne, L.C., Klimczak, R.R., Visel, M., Yin, L., Merigan, W.H., Flannery, J.G. and Schaffer, D.V. (2013) In Vivo-Directed Evolution of a New Adeno-Associated Virus for Therapeutic Outer Retinal Gene Delivery from the Vitreous. *Sci. Transl. Med.*, **5**, 189ra76-189ra76.
52. Körbelin, J., Dogbevia, G., Michelfelder, S., Ridder, D.A., Hunger, A., Wenzel, J., Seismann, H., Lampe, M., Bannach, J., Pasparakis, M., *et al.* (2016) A brain microvasculature endothelial cell-specific viral vector with the potential to treat neurovascular and neurological diseases. *EMBO Mol. Med.*, **8**, 609–625.
53. O'Reilly, M., Palfi, A., Chadderton, N., Millington-Ward, S., Ader, M., Cronin, T., Tuohy, T., Auricchio, A., Hildinger, M., Tivnan, A., *et al.* (2007) RNA Interference–Mediated Suppression and Replacement of Human Rhodopsin In Vivo. *Am. J. Hum. Genet.*, **81**, 127–135.
54. Morabito, G., Giannelli, S.G., Ordazzo, G., Bido, S., Castoldi, V., Indrigo, M., Cabassi, T., Cattaneo, S., Luoni, M., Cancellieri, C., *et al.* (2017) AAV-PHP.B-Mediated Global-Scale Expression in the Mouse Nervous System Enables GBA1 Gene Therapy for Wide Protection from Synucleinopathy. *Mol. Ther.*, **25**, 2727-2742.
55. Pinello, L., Canver, M.C., Hoban, M.D., Orkin, S.H., Kohn, D.B., Bauer, D.E. and Yuan, G.C. (2016) Analyzing CRISPR genome-editing experiments with CRISPResso. *Nat Biotechnol.*, **34**, 695–697.
56. Latella, M.C., Di Salvo, M.T., Cocchiarella, F., Benati, D., Grisendi, G., Comitato, A., Marigo, V. and Recchia, A. (2016) In vivo Editing of the Human Mutant Rhodopsin Gene by Electroporation of Plasmid-based CRISPR/Cas9 in the Mouse Retina. *Mol. Ther. - Nucleic Acids*, **5**, e389.

57. Bakondi, B., Lv, W., Lu, B., Jones, M.K., Tsai, Y., Kim, K.J., Levy, R., Akhtar, A.A., Breunig, J.J., Svendsen, C.N., *et al.* (2015) In Vivo CRISPR/Cas9 Gene Editing Corrects Retinal Dystrophy in the S334ter-3 Rat Model of Autosomal Dominant Retinitis Pigmentosa. *Mol. Ther.*, **24**, 556–563.

58. Ran, F.A., Hsu, P.P.D., Wright, J., Agarwala, V., Scott, D.A. and Zhang, F. (2013) Genome engineering using the CRISPR-Cas9 system. *Nat. Protoc.*, **8**, 2281–2308.

59. McGrew, D.A. and Hedstrom, L. (2012) Towards a pathological mechanism for IMPDH1-Linked retinitis pigmentosa. In *Advances in Experimental Medicine and Biology*, **723**, 539–545.

60. Wen, Y., Locke, K.G., Klein, M., Bowne, S.J., Sullivan, L.S., Ray, J.W., Daiger, S.P., Birch, D.G. and Hughbanks-Wheaton, D.K. (2011) Phenotypic characterization of 3 families with autosomal dominant retinitis pigmentosa due to mutations in KLHL7. *Arch. Ophthalmol.*, **129**, 1475–82.

61. Swiech, L., Heidenreich, M., Banerjee, A., Habib, N., Li, Y., Trombetta, J., Sur, M. and Zhang, F. (2015) In vivo interrogation of gene function in the mammalian brain using CRISPR-Cas9. *Nat Biotechnol*, **33**, 102–106.

62. Cho, S.W., Kim, S., Kim, Y., Kweon, J., Kim, H.S., Bae, S. and Kim, J. (2014) Analysis of off-target effects of CRISPR/Cas-derived RNA-guided endonucleases and nickases. *Genome Res.,* **24**, 132-141.

63. Tsai, S.Q., Zheng, Z., Nguyen, N.T., Liebers, M., Topkar, V. V, Thapar, V., Wyvekens, N., Khayter, C., Iafrate, A.J., Le, L.P., *et al.* (2015) GUIDE-seq enables genome-wide profiling of off-target cleavage by CRISPR-Cas nucleases. *Nat Biotechnol.*, **33**, 187–197.

64. Wang, X., Wang, Y., Wu, X., Wang, J., Wang, Y., Qiu, Z., Chang, T., Huang, H., Lin, R. and Yee, J. (2015) Unbiased detection of off-target cleavage by CRISPR-Cas9 and TALENs using integrase-defective lentiviral vectors. *Nat Biotechnol.*, **33**, 175–178.

65. Merienne, N., Vachey, G., de Longprez, L., Meunier, C., Zimmer, V., Perriard, G., Canales, M., Mathias, A., Herrgott, L., Beltraminelli, T., *et al.* (2017) The Self-Inactivating KamiCas9 System for the Editing of CNS Disease Genes. *Cell Rep.*, **20**, 2980–2991.

66. Shin, J., Jiang, F., Liu, J.J., Bray, N.L., Rauch, B.J., Baik, S.H., Nogales, E., Bondy-Denomy, J., Corn, J.E. and Doudna, J.A. (2017) Disabling Cas9 by an anti-CRISPR DNA mimic. *Sci. Adv.*, **3**, e1701620.

67. Caiazzo, M., Giannelli, S., Valente, P., Lignani, G., Carissimo, A., Sessa, A., Colasante, G., Bartolomeo, R., Massimino, L., Ferroni, S., *et al.* (2015) Direct conversion of fibroblasts into functional astrocytes by defined transcription factors. *Stem Cell Reports*, **4**, 25–36.

68. Vierbuchen, T., Ostermeier, A., Pang, Z.P., Kokubu, Y., Thomas, C.S. and Wernig, M. (2010) Direct conversion of fibroblasts to functional neurons. *Nature*, **77**, 7–8.

69. Giannelli, S.G., Demontis, G.C., Pertile, G., Rama, P. and Broccoli, V. (2011) Adult human Müller glia cells are a highly efficient source of rod photoreceptors. *Stem Cells*, **29**, 344–356.

70. Langmead, B., Trapnell, C., Pop, M. and Salzberg, S. (2009) Ultrafast and memory-efficient alignment of short DNA sequences to the human genome. *Genome Biol.*, **10**, R25.

71. Back, S.H., Lee, K., Vink, E. and Kaufman, R.J. (2006) Cytoplasmic IRE1alpha-mediated XBP1 mRNA splicing in the absence of nuclear processing and endoplasmic reticulum stress. *J. Biol. Chem.*, **281**, 18691–18706.

72. Pinto, L.H., Vitaterna, M.H., Siepka, S.M., Shimomura, K., Lumayag, S., Baker, M., Fenner, D., Mullins, R.F., Sheffield, V.C., Stone, E.M., *et al.* (2004) Results from screening over 9000 mutation-bearing mice for defects in the electroretinogram and appearance of the fundus. *Vision Res.*, **44**, 3335–3345.

73. Brandli, A. and Stone, J. (2015) Using the electroretinogram to assess function in the rodent retina and the protective effects of remote limb ischemic preconditioning. *J. Vis. Exp.*, **9**, e52658.

Figure Legends

Figure 1. *In vivo* analysis of sgRNA-mut effect on the *Rho*^{P23H} and *Rho*^{WT} alleles. Experimental work-flow of the *in-vivo* study. *Rho*$^{P23H/+}$ retinae were electroporated at P0 (left panel) with two pCAG expression vectors: one expressing the VQR variant of the SpCas9 together with the sgRNA-mMUT and the other an EGFP cassette. EGFP fluorescence was instrumental for the recovery upon FACS sorting (right panel) of the transduced cells (central panel). After cell sorting, selective PCRs utilized for amplification of P23H and wild-type (WT) *Rho* alelles. Amplicons were subjected to a panel of cleavage assay (A). Analysis of indel mutations by the T7EI assay in P23H *Rho* (B) (n=4) and WT alleles (C) (n=5) in electroporated and non electroporated retinae (NE)..TIDE analysis of representative retinal samples for P23H (D) and WT (E) *Rho* alleles indicating predicted indel efficiency. Clone sequencing analysis for the determination of the indel mutation on P23H (F) (n=40) and WT (G) (n=36) *Rho* alleles of electroporated retinae. The most frequent sequence found at the level of the P23H *Rho* allele was p.P23QfsX3, produced by the insertion of an adenine (A) nucleotide in position 68 (H), whereas the unaltered sequence was the most represented at the level of the WT allele of electroporated retinae. Quantification of the indel rate (J, L) and frameshift mutation recurrence (G, M) in P23H Rho (J, K) and wild-type (WT) (L, M) of electroporated retinae.

Figure 2. Overexpression in P19 cells of the different variants of the WT, P23H and edited. mRho alleles. Schematic view of the different mRho gene variants tested. From left to right: map of the pCAG-ires-EGFP vector used to over-express all variants and their description at the DNA and protein level (A). Co-localization of ectopic EGFP and Rhodopsin in P19 cells transduced with an empty vector, or carrying WT, mutated P23H or edited Indel A or Indel B Rho alleles. EGFP^{+} cells were tested for co-localization with two different rhodopsin antibodies: one at the N-terminus (monoclonal RET-P1 red) and the other at the C-terminus (polyclonal, purple). While the WT and P23H Rhodopsin proteins were detected respectively on the cell membranes and intracellularly, IndelA and IndelB did not produce any detectable Rhodopsin protein staining (B). Bar: 10 μm.

Figure 3. Histological analysis of *Rho*$^{+/P23H}$ mutant retinae 1 month after treatment with Cas9-VQR only (control) or together with the sgRNA-mMUT. Representative images of non-electroporated retinae (**A**, Left Eye, LE) and electroporated with the pCAG-GFP construct together with a second vector containing the Cas9-VQR only (**B**, Control) or with a cassette expressing the sgRNA-mMUT (**C**, Treated). ONL thickness didn't differ as quantified (D, n=3). Control retinae (E,F) display

shorter and overall dysmorphic Outer Segments (OS) as compared to CRISPR-VQR treated retinae (G,H) as revealed by EGFP staining and imaged by confocal microscopy at high magnification. Immunofluorescence for the rod OS marker CNGA (red) and the Inner Segment (IS) marker Calnexin (CNX, purple) further highlights the differences between control (I,J) and treated photoreceptors (K,L). OS measurements confirm OS and OS/IS tract preservation (M, n=3, #p<0.05 relative to OS/IS length, *p<0.05 relative to OS length). Merge of EGFP, CNGA and CNX immunofluorescence staining highlighting morphological features of the photoreceptors treated with CRISPR/spCas9-VQR system (N,O) versus control (P,Q). ONL: Outer Nuclear Layer, INL: Inner Nuclear Layer, GCL: Ganglion Cell Layer. Bar: 10 μm. (Error bars indicate SD)

Figure 4. Histological and electrophysiological recordings in control and CRISPR/Cas9 treated retinae at 3 months. Representative images of both non-electroporated (A, Left Eye) retinae and electroporated with the pCAG-GFP construct together with a second vector containing the Cas9-VQR only (B, Control) or with a cassette expressing sgRNA-mut (C, Treated). ONL thickness quantification (D, n=3) indicated a significantly ONL rescue in Treated compared to Control retinae (Error bars indicate SD, *p<0.05, Error bars indicate SD). (E,F) which is partially preserved in treated rod photoreceptors (G,H). Immunofluorescence labelling of the IS (CNX, purple) or the OS (CNGA, red) uncovering subcellular structures in control (I,J) and treated retinae (K,L). OS measurements confirm OS and OS/IS tract preservation (M, n=3, #p<0.05 relative to OS/IS length, *p<0.05 relative to OS length, Error bars indicate SD). Merge of GFP, CNX and CNGA immunofluorescence staining in control (N,O) and CRISPR treated retinae (P,Q). ONL: Outer Nuclear Layer, INL: Inner Nuclear Layer, GCL: Ganglion Cell Layer. Scale bar: 10 μm (A-N). Representative ERG traces recorded simultaneously from left (LE) and right (RE) eyes of WT (R) (n=10), Cas9 VQR only (S) (n=12) and Cas9 VQR + SgRNA-mMUT (T) (n=14) treated $Rho^{+/P23H}$ mice. Each sweep is the average of 6 trains of 10 flashes, delivered at time 0 (red line). Histograms show ERG a-wave (U) and b-wave (V) amplitude normalized on those from non-electroporated LEs. Error bars indicate SEM. *p<0.05; **p<0.01.

Figure 5. Intravitreal (IV) injection of the AAV-PHP.B transduces the whole retina and the ONL with high efficiency. (A) Schematic description of the experimental setting. 2 weeks after IV injection (1μL of $1x10^{12}$ viral genomes/mL, vg/mL) transgene expression was strongly detected in the retina as shown in the entire tissue (B) or a representative section (C). Confocal images indicated strong transduction of the RPE (D) and various retinal cell types (E), such as both photoreceptors, both rod (F) and cones (G), ganglion cells (GC) (F), amacrine cells (AC) (G),

horizontal cells (HC) (K), Muller glia cells (MG) (L). Quantification of the percentage of cells positive for GFP□2 weeks after retinal IV injection (M). Scale bars: in (B) and (C): 100 μm; in (D) and (F): 20 μm; in (E-L): 20 μm.

Figure 6. AAV-PHP.B-mediated targeting of *Rho*$^{+/P23H}$ whole retinae. (A) Schematic view of AAV vectors injected IV (0,5μL of 1x10^{12} vg/mL of each AAV preparation). (B) Rhodopsin promoter was employed to restrict GFP and rtTA expression to photoreceptors thus ensuring Cas9-VQR activation solely in this retinal sub-population Scale Bar: 20 μm. 2 weeks after injection (0,5μL of 1x10^{12} vg/mL of each AAV preparation) retinae were sorted and genome editing tested. Indel quantification using T7EI assay was performed on GFP^{+} FACS-sorted retinae in order to detect indels at the level of the P23H *Rho* allele (C) or the WT allele (D). (E) Based on FACS analysis two distinct populations of GFP^{+} cells were identified and sorted: GFP-low and GFP-high. Indel analysis, as measured by T7EI assay, was performed on GFP-high and GFP-low fraction of two injected retinae at the level of the P23H *Rho* (F) and WT *Rho* allele (G). Using TIDE analysis we observed an even greater clustering of the editing events in the GFP-high fraction (I) compared to the parental GFP^{+} fraction (H) for the P23H *Rho* allele.

Figure 7. NGS analysis of AAV-PHP.B injected and electroporated retinae. Description of retinal samples analyzed in regards to the type of transduction, the transduced constructs and the type of FACS-sorting employed (A). Quantification of allele frequency of the unmodified allelles: *Rho*^{P23H} (red) and *Rho*^{WT} (blue), and the edited alleles, presenting either with deletion (green, DEL) or insertion (yellow, INS) in retinal samples (B). Frame-shift analysis of indels in retinal samples (C). Out-of-frame mutations (dark and light blue, respectively +2 and +1) greatly overcome in-frame mutations (red, +3).

Figure 8. CRISPR/Cas9 selective targeting of either WT or P23H *RHO* allele in human cells. Schematic of sgRNA-hWT (green) and sgRNA-hMUT (orange) annealing to their target sequences (upper case), differing for a single nucleotide (underscored). Symbols indicate: *: mismatches, red line: PAM sequence, red triangle: DSB site; colour blue: Pro23, purple: His23 (A). Cleavage efficiency as measured with T7EI assay. T7EI assay performed on *RHO*$^{+/+}$ (B,C) (n=3) and *RHO*$^{P23H/P23H}$ (D,E) (n=3) 293T cells resulted in detectable DNA cleavage only when complementarity between sgRNA and target sequence was perfect. TIDE analysis on *RHO*$^{+/+}$ cells with sgRNA-hWT (F) showed greater cleavage than sgRNA-hMUT (G) and *vice versa* on *RHO*$^{P23H/P23H}$ cells with sgRNA-hMUT (I) showed greater cleavage than sgRNA-hWT (H) (R^2

indicates the variance, a statistic value of likelihood of the TIDE prediction). Molecular cloning followed by Sanger sequencing indicated the presence of various sgRNA-hWT targeted sequences in *RHO*$^{+/+}$ cells (J,N,R) (n=31) presenting high rate of frameshift (R) but not on *RHO*$^{P23H/P23H}$ cells (L,P,T) (n=22) conversely when sgRNA-hMUT was applied to *RHO*$^{+/+}$ cells no indel mutations were detected (K,O,S) (n=24) where they were present in *RHO*$^{P23H/P23H}$ cells (M,Q,U) (n=35) resulting in a high rate of frameshift mutations (U). *$p<0.05$.

Supplementary Information

Supplementary Figure 1. Conservation of PAM sequences between the mouse and human P23H Rhodopsin mutant alleles. Schematic view of the Rhodopsin gene (A). In both humans (B) and mice (C) the substitution of the cytosine (C) with an adenine (A) (bold) in position 68 causes the missense mutation Pro23Hist (P23H) (purple) responsible for rod cell degeneration. Schematic view of the sgRNA potentially selective for the human P23H Rho allele (B). Schematic view of the sgRNA potentially selective for the murine P23H Rho allele and conserved in humans (C). DBS (triangle) and PAM domains (line) of the different guides are coloured according PAM specificities as indicated by the legend. NGG: SpCas9 (WT), NGA: SpCas9-VQR, NGCG: SpCas9-VRER, NGGRRT: SaCas9 (WT), NNHRRT: SaCas9-KHH. NAAAAC TdCas9, NNACAAW StCas9 e NNNNGATT NmCas9 SgRNA used in this work are indicated with the name that we used throughout the manuscript. Other RHO gene mutations associated with adRP that can be targetable selectively by the CRISPR/Cas9 system.

Supplementary Figure 2. SaCas9 selective sgRNA targeting in *Rho*$^{+/+}$ and *Rho*$^{P23/}$P23H MEFs. MEFs were transduced with the sgRNA-saC1 and sgRNA-saC2 together with the vector for SaCas9-KHH-puro expression. Indel analysis was performed with T7EI assay (A). SaCas9-KHH-puro construct was further validated with a third guide published for targeting the hEMX1 locus in 293T cells (**B**). Quantifications indicated at the bottom of each lane are based on the ratio between cleaved bands (red asterisks) and the top uncleaved band (blue asterisk). TIDE analysis of MEFs indicating predicted indel efficiency in Rho$^{+/+}$ and Rho$^{P23H/P23H}$ (C) and 293T cells (D) R^2 indicates the variance, a statistic value of likelihood of the TIDE prediction.

Supplementary Figure 3. *In vitro* selectivity of the sgRNA-mut for *Rho*^{P23H} but not for *Rho*^{WT}. Schematic of sgRNA-mMUT interaction with *Rho*$^{+/+}$ (A) and *Rho*$^{P23/P23H}$ (B) allele. The substitution of the cytosine (C) into adenine (A) in position 68 (bold) of the *Rho* DNA sequence causes at the aminoacidic level a Pro (blue) to His (purple) change in position 23. The mutation falls in close proximity to the DBS (red triangle) targeted by the sgRNA-mMUT (orange), predicted 3nt upstream of the PAM domain (CGA, red). sgRNA-mMUT was designed to anneal perfectly the mutated sequence (B) but presents a single mismatch (A, orange asterisk) when annealing the wild-type sequence that falls directly into its seed-sequence (orange line). Indel analysis with T7EI assay was performed on *Rho*$^{+/+}$ (C) and *Rho*$^{P23H/P23H}$ (D) MEFs, transduced with a single lentiviral vector carrying the sgRNA-mMUT and SpCas9-VQR (Cas9-sgRNA) or with multiple vectors in order to combine them not only with each other but also respectively with the unaltered SpCas9 (WT) and an uspecific sgRNA (US) that targets a canonic NGG PAM. T7EI assay quantification is indicated at the bottom of each lane and is based on the ratio between cleaved bands (red asterisks) and the top uncleaved band (blue asterisk)**.** TIDE analysis indicates predicted indel efficiency of *Rho*$^{+/+}$ (E) and *Rho*$^{P23H/P23H}$ MEFs representative samples (F). R^2 indicates the variance, a statistic value of likelihood of the TIDE prediction. Indel rate was measured by clone sequencing for both *Rho*$^{+/+}$ (G) (n=40) and *Rho*$^{P23H/P23H}$ (H) (n=45) CRISPR-treated MEFs.Representative indel occurred in *Rho*$^{P23H/P23H}$ MEFs (I).

Supplementary Figure 4. Analysis of off-target candidate sites. The 4 most likely off-target genomic sites are listed with their chromosomes (Chr), sequences (target sequence in white, mismatches respect to target sequence in red and PAM sequence underscored), number of mismatches and scores according to the web-tool COSMID (https://crispr.bme.gatech.edu). Chromatograms (PAM are indicated with a black line) and relative TIDE analysis are indicated for each off-target. R^2 indicates the variance, a statistic value of likelihood of the TIDE prediction. This analysis was performed on Rho$^{P23H/P23H}$ MEFs treated with sgRNA-mMUT and SpCas9-VQR (A) and on P23H Rho allele of heterozygous retinae$^{+/P23H}$ electroporated with sgRNA-mMUT and SpCas9-VQR (B).

Supplementary Figure 5. Optimization of PCRs selective for either the WT or the P23H *Rho* allele. Chromatograms of Rhodopsin gDNA of *Rho*$^{+/+}$ (top) and *Rho*$^{P23H/P23H}$ (bottom) MEFs in two different genomic region: +60/+80bp downstream (were c.68C>A falls, blue vs. purple) and -200/-180bp upstream of the ATG were a second discontinuity in linkage disequilibrium was observed (blue vs. purple). Arrows indicate selective forward primers used to amplify specifically WT (blue)

or P23H *Rho* (purple) allele (A). Tm (melting temperature) optimization for the WT (PCR-WT) or P23H *Rho* (PCR-P23H) allele amplification using gDNA from $Rho^{P23H/P23H}$, $Rho^{+/P23H}$ and $Rho^{+/+}$ cells (B). Chromatograms of PCR-WT and PCR-P23H products performed on gDNA from $Rho^{+/P23H}$ at basic and optimised temperature (C). Schematic view of the BanII RFLP used to discriminate between WT (bottom) and P23H (top) Rho allele, * c.68C>A mutation (D). PCR-P23H (E) and PCR-WT (F) products were cloned into pCR4 vector (clone 1 to 18) in order to verify the presence of the respective products (also included as control E, 10^{th} lane and F**,** 11^{th} lane) using BanII digestion. *Clones carrying the unwanted product subjected to sequencing for further confirmation.

Supplementary Figure 6. Employment of allele selective PCRs to analyse the specific cleavage of sgRNA-mWT and sgRNA-mMUT on heterozygous $Rho^{+/P23H}$ MEFs. Schematic view of sgRNA-mWT (green) and sgRNA-mMUT (orange) binding to the WT and P23H Rho alleles (uppercase) (A). *, mismatches. Red line, PAM sequence. Red triangle, DSB site. Colour blue, Proline (Pro). Purple: Histidine (His). T7EI assay on PCR-WT amplicons from heterozygous cells treated with sgRNA-mWT, sgRNA-mMUT and no sgRNA and its quantification (n=3) on PCR-WT (B,C) as well as on PCR-P23H amplicons (D,E). TIDE analysis of representative samples obtained using either PCR-WT amplicons on heterozygous MEFs treated with sgRNA-mWT (F) and sgRNA-mMUT (G) or PCR-P23H amplicons on cells treated with sgRNA-mWT (H) and sgRNA-mMUT (I). R^2 indicates the variance, a statistic value of likelihood of the TIDE prediction. Molecular cloning followed by Sanger sequencing indicates the presence of indel when PCR-WT amplification was applied to sgRNA-mWT-treated heterozygous MEFs (n=18) (J,N), but not using PCR-P23H amplification (n=10) (L,P). Conversely when PCR-WT amplification was applied to sgRNA-hMUT-treated heterozygous MEFs no indel mutations were detected (n=10) (K-O), but they were present in PCR-P23H amplified products (n=10) (M,Q). *$p<0.05$

Supplementary Figure 7. Rho mRNA levels and UPR stress induced by ectopic expression of the different Rho alleles *in vitro.* RNA quantification by qPCR of the different Rho alleles overexpressed in P19 cells (n=3, *$p<0.05$ from pCAG-Rho-WT; #$p<0.05$ from pCAG-Rho-P23H) (A). cDNAs used for Rho qPCR were tested for plasmid DNA contamination by RT-PCR targeting the CAG promoter of the plasmid backbone Plasmid DNA (pl) is also included as positive control (B). Schematic view of the Xbp splicing reporter (C). Representative images of P19 cells transduced with the *Xbp1* reporter together with the 3 different WT (D), P23H (E) and the IndelA (F) Rho alleles. FACS–based quantification of GFP positive cells transduced with the *Xbp1* reporter

together with the empty pCAG vector or overexpressing different Rho alleles. (n=3, *p<0.05 from empty vector) (G). qPCRs assay to quantify the *Xbp1* spliced (s) and unspliced (u) transcript variants (the asterisk indicates the position of a hybrid amplicon) in cells untrasfected and untreated (NT), untransfected but treated with Tunicamicin (Tun, 5□g/mL), mock transfected with GFP construct and finally with different Rho alelles (*Rho*). Spliced *Xbp1* fraction quantification is indicated at the bottom (H).

Supplementary Figure 8. Immunohistochemical characterization of *Rho*$^{+/P23H}$ mutant retinae 1 month or 3 month after treatment with Cas9-VQR only (Control) or together with the sgRNA-mMUT (Treated). Hoechst staining imaging was performed to better appreciate layers thickness (A-D). Rhodopsin delocalization was probed in all conditions (E-H). Cone presence was detected with a Red-Green Opsin immunoreactivity (I-L). Microglia characterization of retinal sample through Iba1 antibody (M-P). Müller glia reactivity detected by GFAP staining (Q-T). Bar: 10 µm.

Supplementary Figure 9. Retinal transduction of retinae injected with 7m8 intravitreal injections. 2 weeks after IV injection of CBA-GFP particles (1µL of 1x10^{12} vg/mL) transgene expression was only weakly detected in the whole retina (A) and upon cryo-sectioning in low (B) and high magnification captures. Confocal images indicated transduction of few retinal cell types (D), such as Muller glia cells (E) and amacrine cells (F). Schematic view of AAVs injected IV (1µL of 1x10^{12} vg/mL) (A). The 7m8 serotype was utilized to produce AAV-Cas9-VQR and AAV-sgRNAMUT-RHOprom-GFP-t2a-rtTa particles that were injected IV in 3-4 weeks old mice. GFP expression in retinae 2 weeks after injection (0,5µL of 1x10^{12} vg/mL of each AAV preparation) (G)
Indel quantification using T7EI assay was performed on GFP^{+} FACS-sorted retinae in order to detect indels at the level of the P23H *Rho* allele or the WT allele (H).

Supplementary Figure 10. Quantification of indel frequency in representative AAV injected retina (A1, A) and electroporated retinae (E1, B). Out-of-frame mutations (dark and light blue, respectively +2 and +1) greatly overcome in-frame mutations (red, +3). In both samples the insertion of a single nucleotide (+1) is by far the most frequent mutation.

Supplementary Figure 11. List of most frequent alleles in representative AAV injected retina (A1, A) and electroporated retinae (E1, B). Substitutions (bold), insertions (□) and delitions (-), respect to P23H *Rho* allele, are indicated. Predicted cleavage position is represented with a black dashed line. For each allele frequency (% of total reads) and number of read are listed on the right.

Supplementary Figure 12. Generation of a stable *RHO*$^{P23H/P23H}$ 293T cell line by CRISPR/Cas9 genome editing. Schematic view of the recombining elements. sgRNA-REC (grey), binds the RHO first exon in proximity of Pro23 (underscored) that overlaps perfectly with its PAM domain (red). Recruitment of the SpCas9 produces a DBS (red triangle) that is repaired either thorough NHEJ or, in presence of the ssODN-donor, by HDR. ssODN-mediated repair introduces mutations at the level of two different nucleotides: c.68C>A, introducing the P23H substitution at aminoacidic level (purple) and c.75G>A, a silent mutation at the level of 25th glutammate residue. This last mutation introduces a BstBI site (black line) in the genomic DNA useful for the identification of the correct recombined clones (A). RFLP analysis shows that clone 12 is fully sensitive to BstBI digestion indicating that both alleles are recombined (B), as subsequently confirmed by Sanger sequencing (C).

Supplementary Figure 13. Representative *RHO* gene mutations associated with adRP selectively targetable by the CRISPR/Cas9 system. For each RHO mutant sequence it is indicated the PAM domain with a colour code for the specific Cas9 variant and overlapping or near the disease mutated nucleotide change (upper case).

Supplementary Table 1. Absolute (expressed in μV) and normalized (expressed in %) ERG amplitudes measured from left (LE) and right (RE) eyes in WT (n=10), Cas9 VQR only (n=12) and Cas9 VQR + Sg RNA mMUT mice (n=14). Values are reported as mean ± SEM.

Figure 1

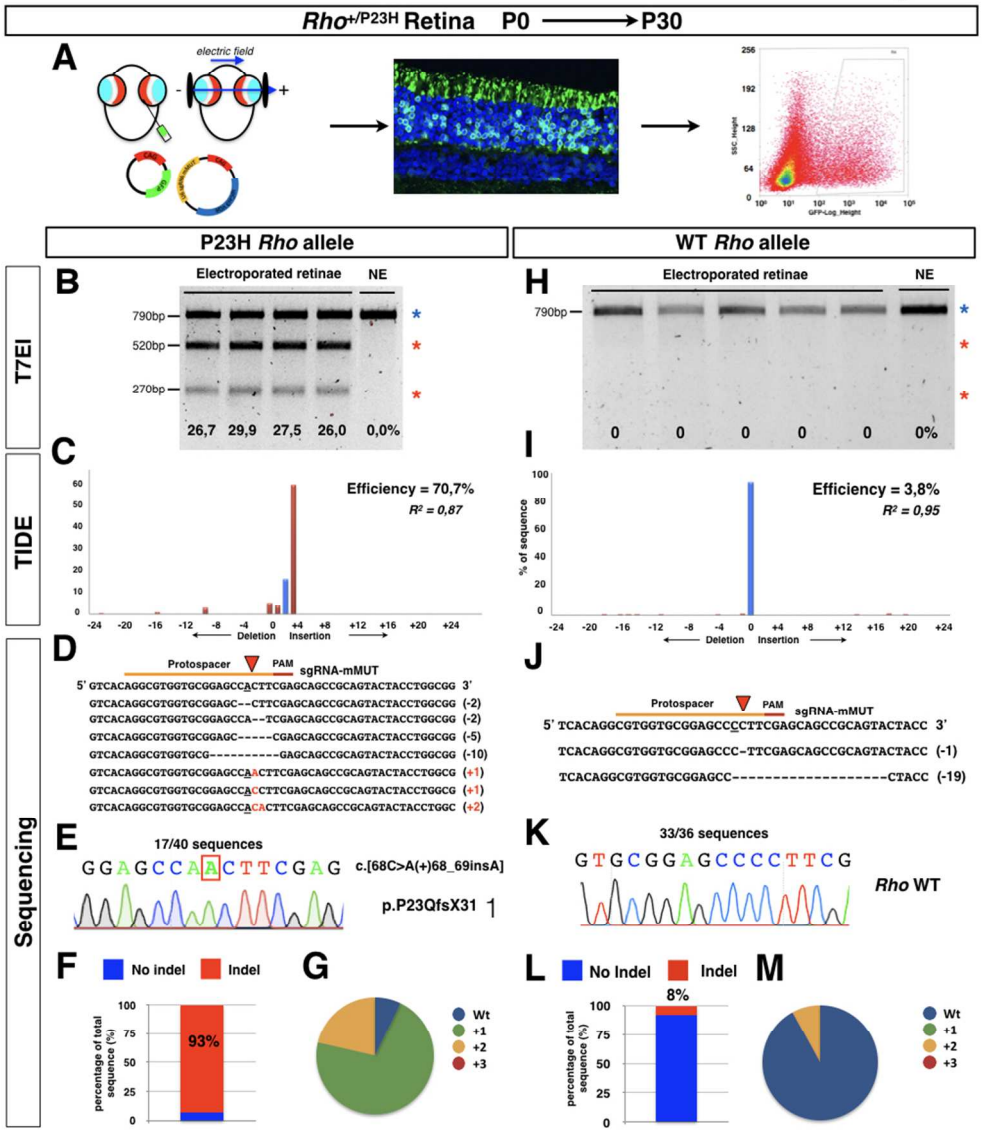

361x423mm (72 x 72 DPI)

Figure 2

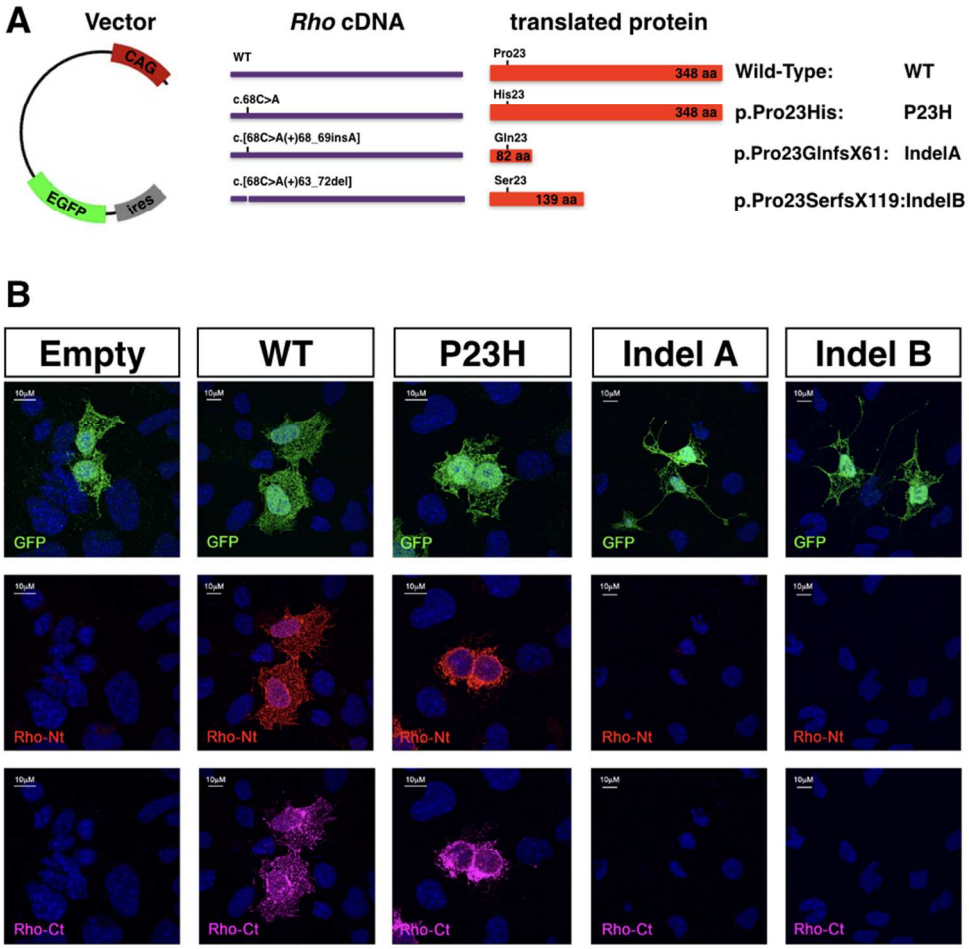

361x423mm (72 x 72 DPI)

Figure 3

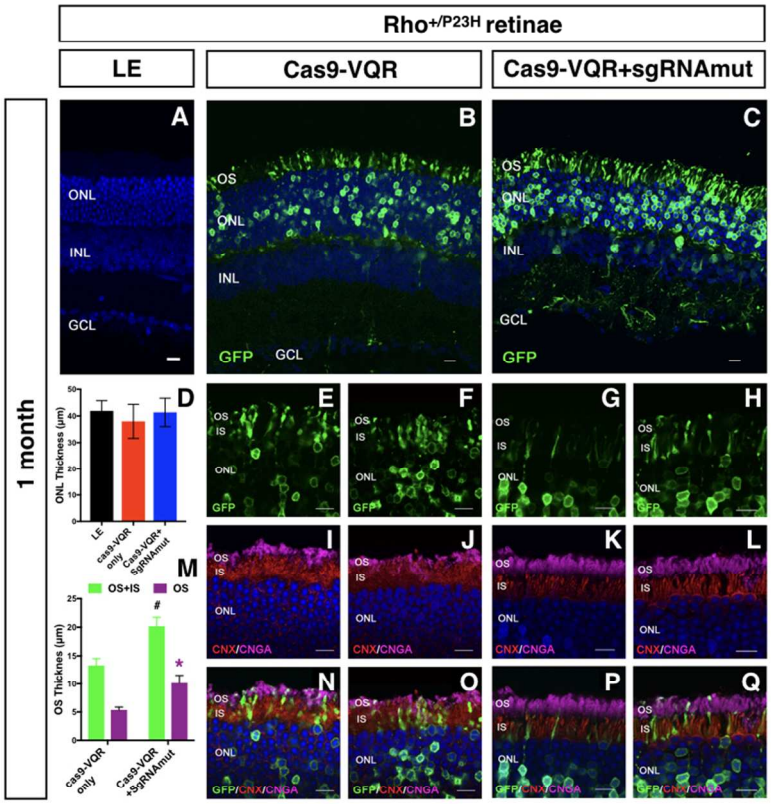

361x423mm (72 x 72 DPI)

Figure 4

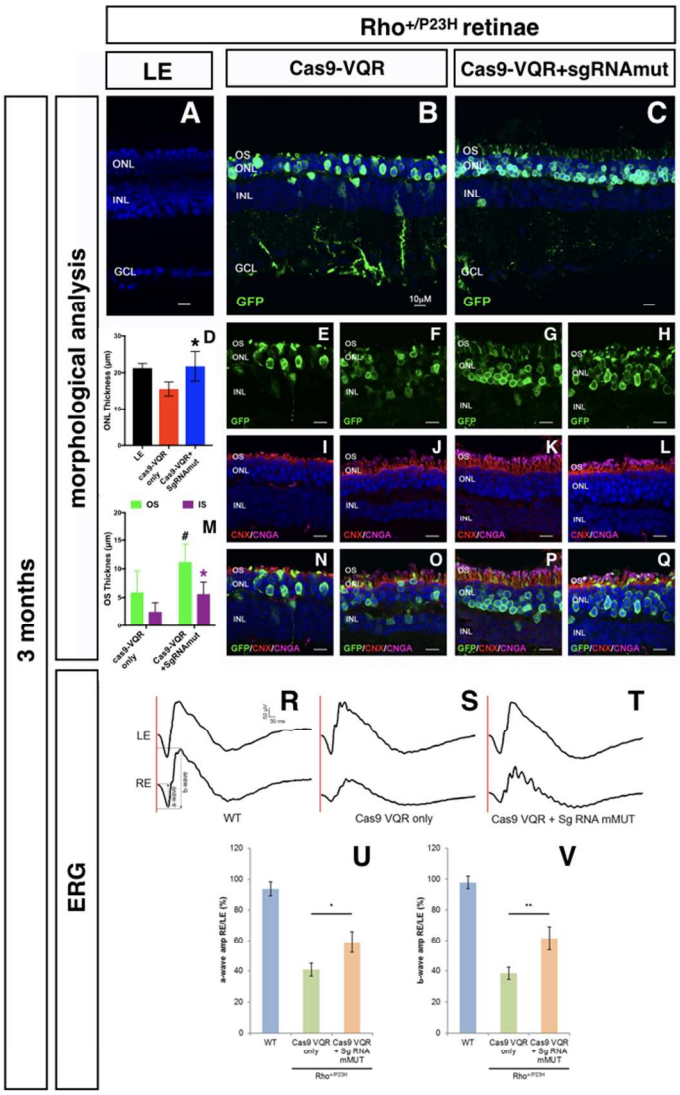

361x423mm (72 x 72 DPI)

Figure 5

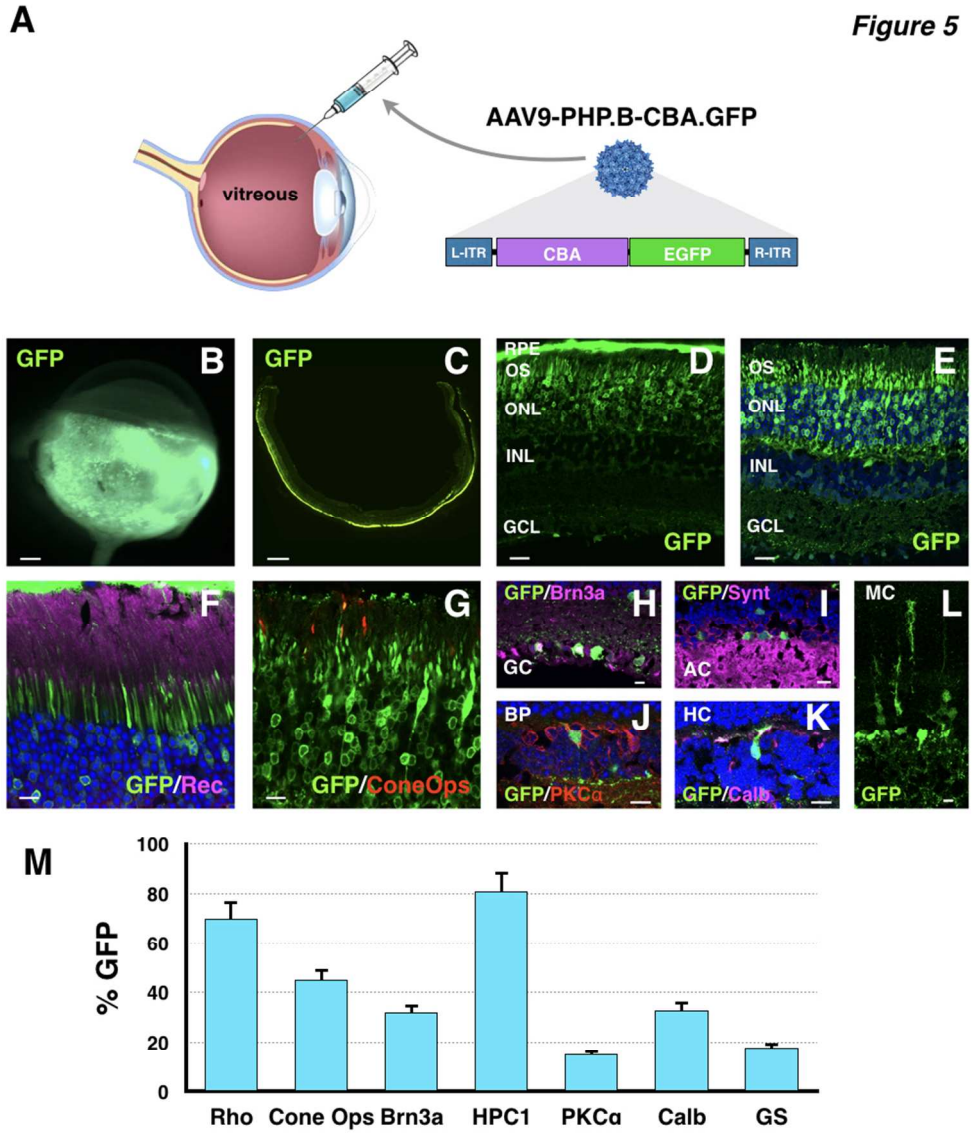

361x423mm (72 x 72 DPI)

Figure 6

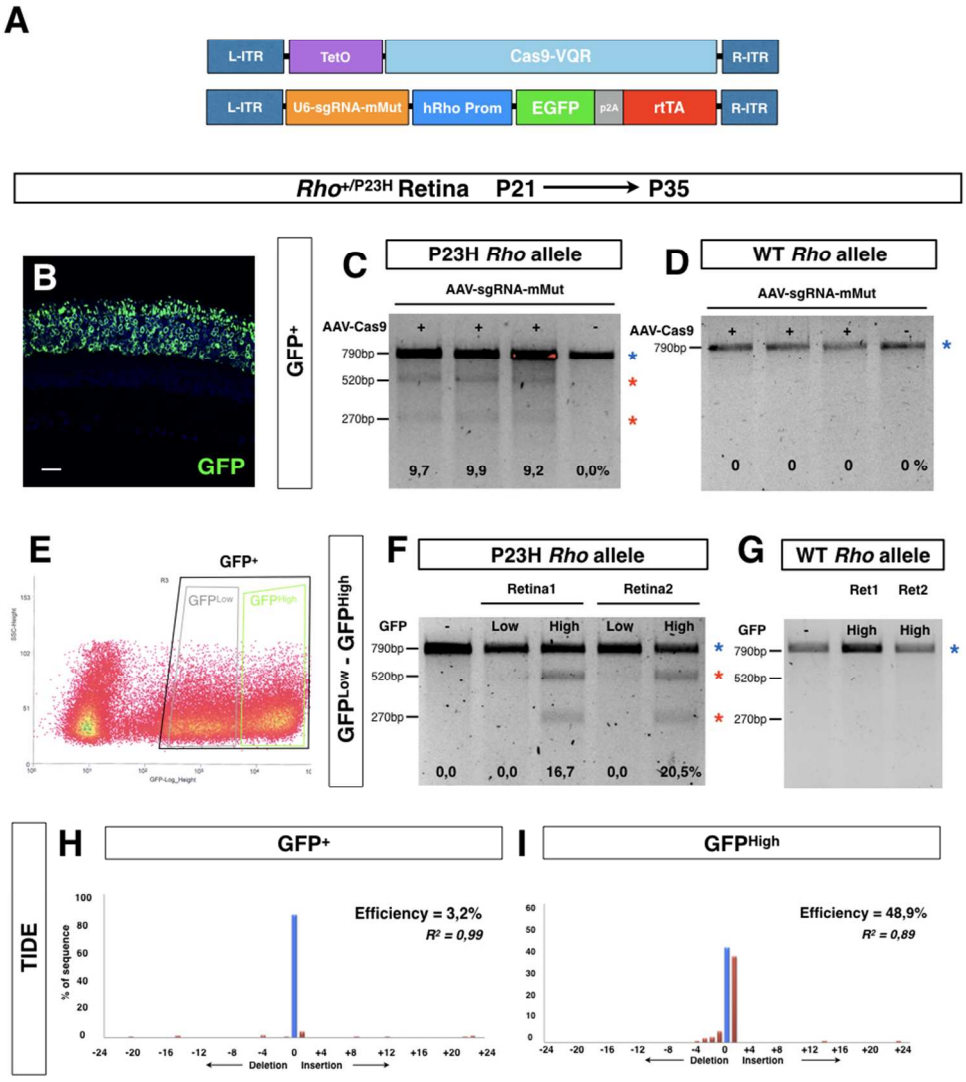

361x423mm (72 x 72 DPI)

Figure 7

A

sample	genotype	type of transduction	constructs	sorting
Cont	*Rho*$^{+/P23H}$	None	None	None
A1	*Rho*$^{+/P23H}$	AAV injection	1: Teto-Cas9-VQR + 2: U6-SgRNA-mMUT-hRHOprom-EGFP-p2a-rtTA	GFP^{High}
A2	*Rho*$^{+/P23H}$	AAV injection		GFP^{High}
A3	*Rho*$^{+/P23H}$	AAV injection		GFP^{+}
E1	*Rho*$^{+/P23H}$	Electroporation	1: pCAG-GFP 2: pU6-SgRNA-mMUT-CAG-Cas9-VQR	GFP^{+}
E2	*Rho*$^{+/P23H}$	Electroporation		GFP^{+}

B

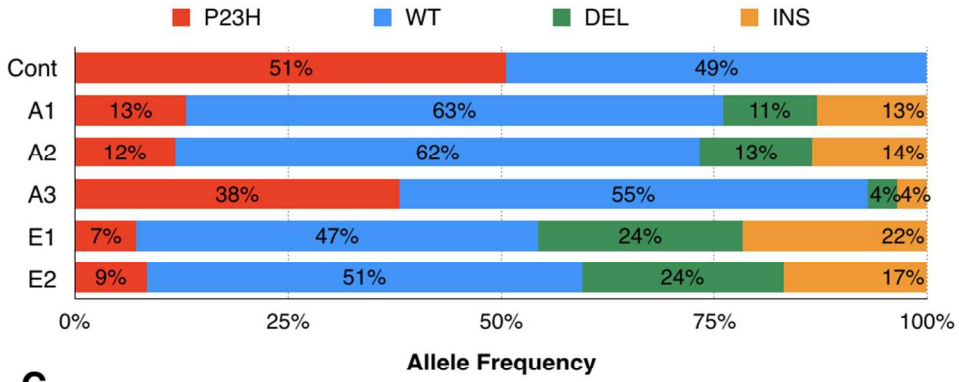

C

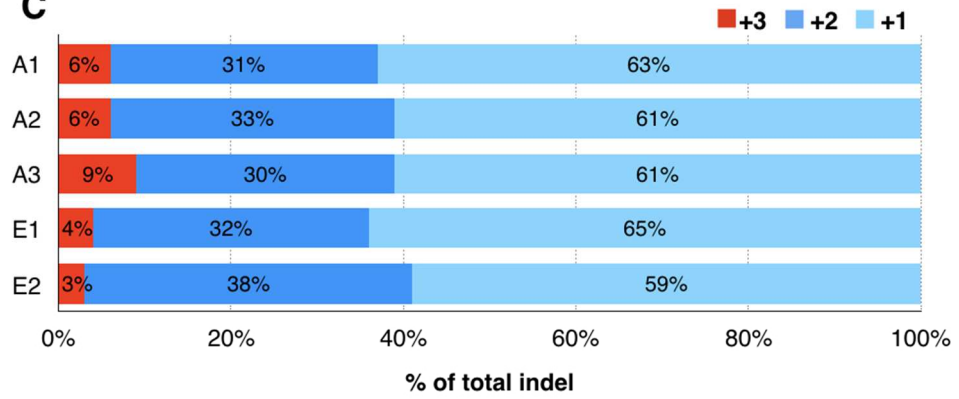

361x423mm (72 x 72 DPI)

Figure 8

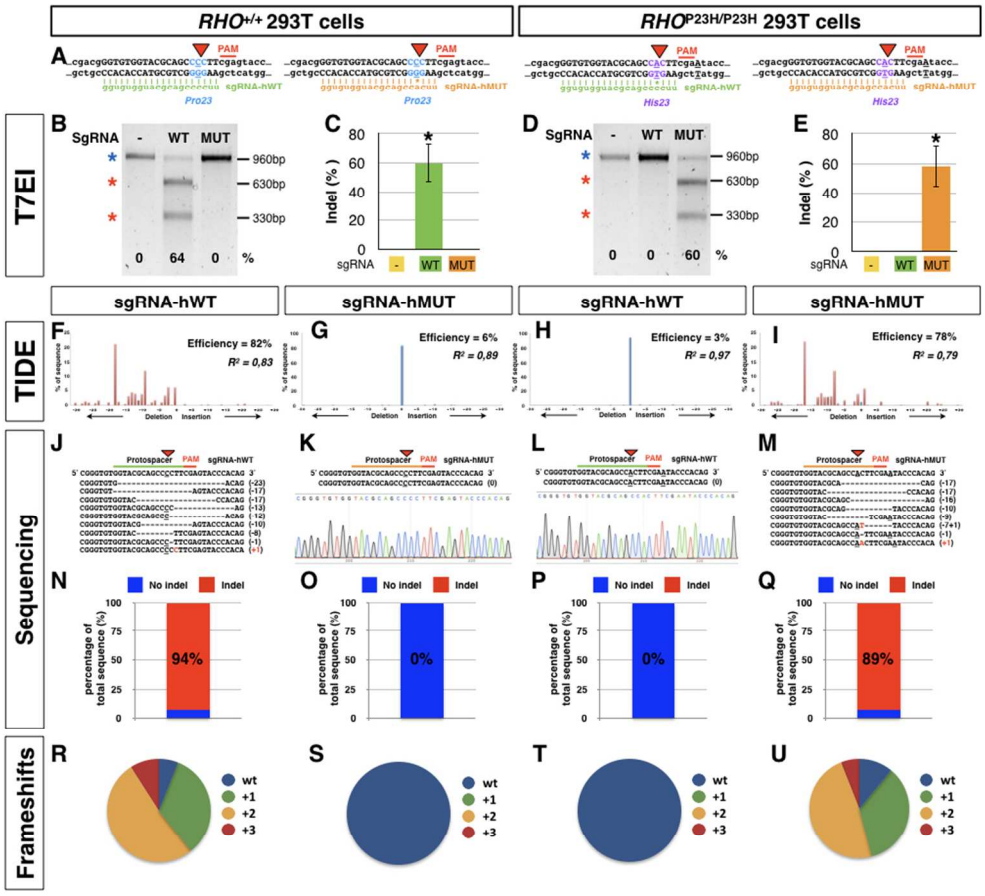

361x423mm (72 x 72 DPI)